JGR Solid Earth

RESEARCH ARTICLE
10.1029/2025JB033101

Mantle Dynamic Topography of the Fringing Oceanic Basins of Antarctica

A. C. A. Dunn[1,2], **N. J. White**[1], **R. Larter**[2], **P. L. Slay**[1], **and M. C. Holdt**[1]

[1]Bullard Laboratories, Department of Earth Sciences, University of Cambridge, Cambridge, UK, [2]British Antarctic Survey, Cambridge, UK

Key Points:

- 1,120 residual depth anomaly measurements from the Southern Ocean
- These anomalies correlate with upper mantle shear wave velocity patterns
- Inferred dynamic topographic support consistent with onshore studies

Supporting Information:

Supporting Information may be found in the online version of this article.

Correspondence to:

A. C. A. Dunn,
aisdunn@bas.ac.uk

Citation:

Dunn, A. C. A., White, N. J., Larter, R., Slay, P. L., & Holdt, M. C. (2026). Mantle dynamic topography of the fringing oceanic basins of Antarctica. *Journal of Geophysical Research: Solid Earth*, *131*, e2025JB033101. https://doi.org/10.1029/2025JB033101

Received 30 SEP 2025
Accepted 27 FEB 2026

Author Contributions:

Conceptualization: N. J. White
Data curation: A. C. A. Dunn
Formal analysis: A. C. A. Dunn
Investigation: A. C. A. Dunn
Methodology: A. C. A. Dunn, M. C. Holdt
Supervision: N. J. White, R. Larter, M. C. Holdt
Visualization: A. C. A. Dunn
Writing – original draft: A. C. A. Dunn
Writing – review & editing: A. C. A. Dunn, N. J. White, R. Larter, P. L. Slay, M. C. Holdt

Abstract Dynamic mantle processes are known to influence oceanic basins with implications for ocean circulation and climate. This study exploits an interdisciplinary approach to probe present-day mantle and lithosphere beneath Antarctica's fringing oceanic basins to better understand sub-crustal processes and implications for the continental realm. To quantify dynamic topography in the Southern Ocean, observed depth to basement is corrected for isostatic loading to isolate the residual bathymetric signal, a robust proxy for dynamic mantle support. In this way, a comprehensive suite of oceanic residual depth measurements ($n = 1120$) are calculated from seismic reflection profiles in the Southern Ocean. This data set is correlated with free-air gravity anomalies and tomographic models to determine which region of the mantle contributes most significantly to dynamic support, with results indicating the upper 530 and 350 km, respectively. These oceanic observations also provide spatial context for onshore studies, where ice-loading and complex geological histories complicate residual elevation estimates. Rare earth element modeling of Neogene basalt samples links offshore dynamic swells and thinned lithosphere to Marie Byrd Land, the West Antarctic Rift System, and the Transantarctic Mountains, with isolated support beneath the Antarctic Peninsula. This pattern aligns with gravity anomalies and slow shear-wave velocity zones. By refining constraints on dynamic mantle support, these results offer benchmarks for geothermal models, mantle convection simulations, oceanographic studies and ice sheet reconstructions, ultimately improving our understanding of Antarctica's role in global climate evolution.

Plain Language Summary The way in which ice sheets slide across Earth's surface, and how ice sheet margins advance and recede, is highly dependent on how hot it is beneath the ice, and the slope of the landscapes over which it flows. Both of these factors are linked to stirring of warm material in the Earth's interior. In an attempt to understand the extent of such processes in Antarctica, we look for evidence at the surface that there is excessively warm material sitting beneath Earth's outermost layer. This includes finding regions with uncharacteristically high elevations and geologically recent volcanic activity. Complexities in conducting studies onshore mean we focus initially on collecting data in the oceans to provide spatial context for work onshore. Our analysis finds that warm material extends from beneath the ocean to under most of West Antarctica and can be used to understand how landscapes have been influenced through time by Earth's interior processes. In turn, these results impact how we consider the Antarctic Ice Sheet to have evolved through time, and how it will react in a warming world.

1. Introduction

It is widely recognized that dynamic mantle processes exert an influence on overlying topography up to amplitudes of 1–2 km and over wavelengths of 1,000–10,000 km (Hoggard et al., 2016; Holdt et al., 2022; Stephenson et al., 2024). This "dynamic topography" arises primarily due to geodynamic processes, in which heat within the Earth's mantle causes convection and drives transient vertical plate motion (Braun, 2010; Forte & Rowley, 2022; Hager et al., 1985; Jordan, 1978; Moucha et al., 2008; Pekeris, 1935; Richards & Hager, 1984). Exactly what processes result in dynamic topography have been debated. Here we adopt the most encompassing definition which includes not only topography arising directly from convective flow within the mantle, but also that which is the result of the buoyancy induced by such temperature variations, as well as the consequent changes in lithospheric thickness, given that the lithosphere–asthenosphere boundary functions as a thermal boundary layer (Forte et al., 1993).

Dynamic topography provides a unique window into sub-crustal processes, offering critical insights into mantle-lithosphere interactions. Constraining the magnitude, spatial extent, and evolution of dynamic topography is

therefore helpful to understanding these processes. In Antarctica, where ice sheets obscure and modify the underlying terrain, dynamic topography's role in shaping the continent's topographic features remains poorly constrained. Extensive glaciation conceals a diverse range of topographic features, as revealed by ice-penetrating radar data (Figure 1a). The degree to which this topography is dynamically supported by mantle processes, however, remains poorly constrained. To first order, dynamic support is spatially coincident with positive free-air gravity anomalies, slow shear-wave velocity anomalies, thin lithosphere and Neogene (<23 Ma) intraplate basaltic volcanism (Parsons & Daly, 1983; A. M. Forte & Mitrovica, 2001; Moucha et al., 2009; Braun, 2010; Hoggard et al., 2017; Ball et al., 2021; Holdt et al., 2022; Stephenson et al., 2024). For Antarctica, such data sets suggest mantle support of the Antarctic Peninsula, Marie Byrd Land (MBL), and the Transantarctic Mountains (TAM), and potential support of Dronning Maud Land (DML) and the Gamburtsev Subglacial Mountains (Figures 1b–1d).

Here, we primarily consider dynamic topography in the oceanic realm by building on the residual depth database of Holdt et al. (2022). Observed depth to basement from seismic experiments is corrected for isostatic loading to isolate the residual bathymetric signal, a proxy for dynamic mantle support. In this way, a comprehensive suite of oceanic residual depth spot measurements ($n = 2105$) is calculated (Data set S2). These results are then interpreted alongside the free-air gravity anomaly, residual tomographic models, seismic lithospheric thickness, and Rare earth element (REE) modeling of intraplate Neogene basaltic volcanic samples ($n = 364$). This multidisciplinary approach is motivated by three key goals.

First, by expanding the residual depth database, dynamic swells in the Southern Ocean are better delineated and provide constraints for their onshore continuation beneath the Antarctic Ice Sheet. Onshore, the extent of dynamic mantle support influences key boundary conditions in ice sheet models, such as palaeotopography and basal heat flux (Austermann et al., 2015; Fox et al., 2024; Golledge et al., 2015; Hasterok, 2010; Lowe et al., 2024). Due to sparse data coverage, uncertainties associated with ice-sheet loading, and variable ways of modeling the complex architecture of continental lithosphere, existing models of onshore residual elevation show considerable differences across Antarctica (Pappa et al., 2019; Paxman, 2023). Offshore and onshore anomalies globally, however, are largely contiguous (Stephenson et al., 2024). By augmenting the residual depth database, important context for interpretation of onshore anomalies is provided.

Secondly, residual bathymetry plays a key role in climatic and oceanic studies, as interpreting palaeo-shorelines and continental flooding in the context of eustatic sea-level change requires knowledge of transient dynamic topography (Cao et al., 2019; Conrad & Husson, 2009; Moucha et al., 2008; Muller et al., 2008; Rovere et al., 2014). Elsewhere (e.g., beneath the North Atlantic Ocean), periodic mantle upwellings, temporally coherent with climate aberrations, have been used to suggest a causal relationship between mantle processes and climate, in part through changes to oceanic gateways and currents (Conway-Jones & White, 2022). Around Antarctica, dynamic mantle processes may similarly influence the Antarctic Circumpolar Current (ACC), a key driver of global thermohaline circulation (Toggweiler & Samuels, 1995). ACC onset is considered pivotal in reducing meridional heat transfer sufficiently to sustain significant glaciation in Antarctica, as well as being linked to northern-hemisphere polar warming (Kennett, 1977; Toggweiler & Bjornsson, 2000).

Topographic features in the Southern Ocean influence the ACC's fronts, which regulate this heat transport (Gille, 1994; Gille et al., 2016; Martinson, 2012; Nowlin & Klinck, 1986). Southern Ocean fronts typically converge on large bathymetric features (e.g., Southwest Indian Ridge) and remain sparsely distributed over abyssal plains (e.g., Australia-Antarctic basin) (Sokolov & Rintoul, 2009). Proximity of warming ACC fronts to continental shelves positively correlates with ice sheet mass loss due to coupling between continental and oceanic realms (Gille et al., 2016). Hence, changes in the extent of dynamic bathymetric support in the Southern Ocean could be of considerable consequence to the evolution of the ACC, its climate feedbacks, and ice dynamics.

Finally, despite only representing a snapshot of modern day dynamic topography, an augmented residual depth database will facilitate a better understanding of mantle-lithosphere interactions through time, as well as the depths within the mantle from which this topography predominantly arises. Recent decades have seen an increased popularity in using computational models to predict both present-day and past dynamic topography to further investigate consequences of transient mantle processes (e.g., Hager et al. (1985); Steinberger (2007); Conrad and Husson (2009); Yang and Gurnis (2016)). Global compilations of residual depth anomalies benchmark such models but expose deficiencies in their ability to reproduce present-day dynamic topography, bringing into question their use in predicting historic mantle flow (Hoggard et al., 2017; Steinberger et al., 2019). Newer

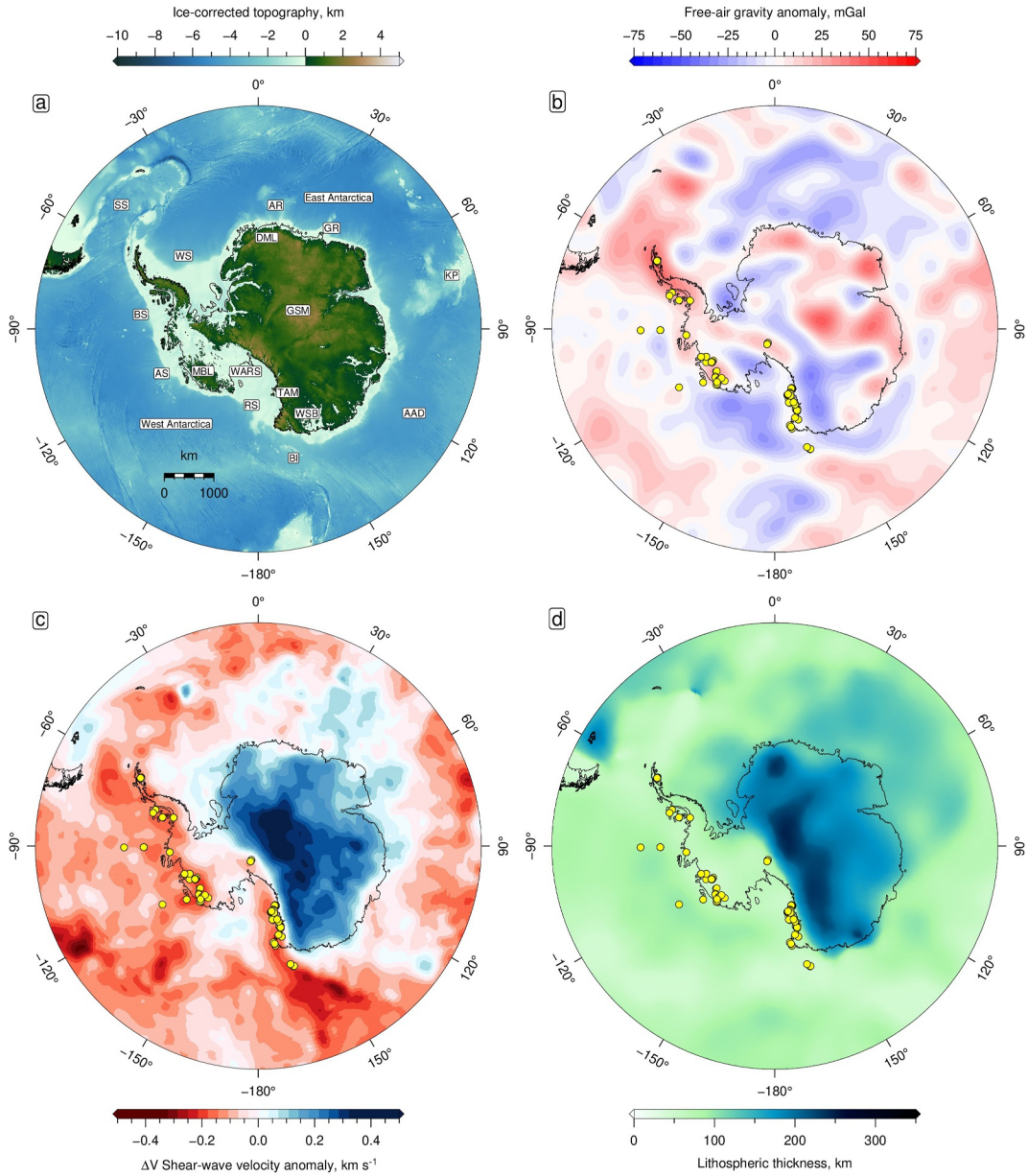

Figure 1. Polar stereographic projection of Antarctic continent. (a) Bedrock topography after Airy-isostatic correction for ice-loading assuming asthenosphere and ice densities of 3.25 Mg m^{-3} and 0.917 Mg m^{-3}, respectively (Morlighem et al., 2020). SS = Scotia Sea; WS = Weddell Sea; BS = Bellingshausen Sea; AS = Amundsen Sea; MBL = Marie Byrd Land; WARS = West Antarctic Rift System; RS = Ross Sea; TAM = Transantarctic Mountains; WSB = Wilkes Subglacial Basin; BI = Balleny Islands; AAD = Australia-Antarctic Discordance; GSM = Gamburtsev Subglacial Mountains; KP = Kerguelen Plateau; DML = Dronning Maud Land; AR = Astrid Ridge; GR = Gunnerus Ridge. (b) GOCO06S free-air gravity anomaly bandpass filtered between spherical harmonic degrees l = 4–55 (730–10,000 km), representative of long-wavelength, non-hydrostatic anomaly (Kvas et al., 2020). Yellow circles = intraplate Neogene volcanism (Data set S1) augmented from Ball et al. (2021), Hole (1988), Hart et al. (1995), Hagedorn et al. (2007), Hole (1990), Hole and LeMasurier (1994), and Panter et al. (2021). (c) ANT-20 relative shear-wave velocity anomaly averaged between 100 and 200 km (Lloyd et al., 2020). (d) Lithospheric thickness (F. Richards, Hoggard, White, & Ghelichkhan, 2020).

studies are now using residual depth measurements to evaluate and improve models (e.g., Brown et al. (2022)), but the relatively sparse coverage of data in the Southern Ocean limits such opportunities in Antarctica.

Increasing observational coverage of residual depth in the region is therefore beneficial not only to quantifying the present day extent of mantle support in the Southern Ocean, but also in enhancing our ability to reconstruct

variations in mantle dynamics over geological time. Such models of mantle convection are essential for defining temporally variable boundary conditions in ice and ocean models, including palaeobathymetry/topography and heat flux, helping elucidate the onset and evolution of the ACC and Antarctic glaciation.

2. Residual Depth Measurements

In the oceans, bathymetric variation primarily results from the cooling and thickening of lithosphere through time (Parsons & Sclater, 1977). Observations show oceanic lithosphere to be largely homogenous, allowing for a clear, age-dependent model of isostatically driven plate subsidence to be established (Crosby et al., 2006; Holdt et al., 2022; Richards et al., 2018; Stein & Stein, 1992). By isolating and removing this isostatic signal from depth to basement observations, global studies consistently show that a fraction of vertical surface deflection, accounting for up to ±1 km of bathymetry, cannot be explained by average trends in plate cooling or variations in crustal or sedimentary thickness and density (Hoggard et al., 2016, 2017; Holdt et al., 2022; Winterbourne et al., 2014). Residual depth anomalies (i.e., deviations from expected subsidence predicted by a plate cooling model) can therefore be used to assess the extent of mantle support or drawdown (Menard, 1973). Collective efforts, culminating in the database of residual depth anomalies presented by Holdt et al. (2022), constitute a comprehensive global study of residual bathymetry, but there is a relative paucity of observations in the Southern Ocean.

2.1. Seismic Database

In order to account for isostatic processes, the effects of sediment and crustal loading of oceanic lithosphere on the observed depth to basement must be corrected for (Menard, 1973). These corrections require accurate quantification of the thickness and density of both the sedimentary and crustal columns. The relationships established by Czarnota et al. (2013) and refined by Holdt et al. (2022) between two-way travel-time (TWTT), thickness, and density for both sediments and crust allow augmentation of the global database in the Southern Ocean through the use of multi-channel seismic (MCS) experiments, made available through the Scientific Committee on Antarctic Research Seismic Data Library Service (Figure 2; SDLS, http://SDLS.ogs.trieste.it). This open archive holds SEG-Y data from seismic reflection surveys surrounding the Antarctic continent, providing a great opportunity to increase the density of residual depth measurements in the region.

The MCS data hosted by the SDLS consistently images the sediment-basement interface which usually produces a strong reflection. The Moho can also be identified in surveys where the fold of coverage is higher, the upper basement horizon is smooth enough to limit scattering of reflections, and/or seabed multiples do not obscure deeper imaging. Figure 3 showcases examples of the data available in the SDLS and how key interfaces are defined for the isostatic corrections.

Four additional wide-angle seismic experiments in which the Moho refracted phase was clearly evident are contributed by this study to the compilation (Table 1, Figure 2). Alongside the lines of Ewing et al. (1971) in the Scotia Sea (SS) which were included in the Holdt et al. (2022) compilation, these experiments provide depth constraints for key interfaces by creating a velocity model of the crust. All reflection and wide-angle experiments are detailed in Data set S3.

By using age models (e.g., Wobbe et al. (2012); Seton et al. (2020)) and magnetic anomalies from the EMAG2 database (Maus et al., 2009), it was ensured only reflection and wide-angle profiles sampling bona fide oceanic crust were interpreted.

2.2. Isostatic Corrections

Having used seismic reflection data to identify the TWTT to the seabed, basement and, where data quality permits, the Moho, methods revised by Holdt et al. (2022) can be used to perform isostatic corrections and determine the water-loaded depth to basement. The method, as summarized schematically in Figure 4, uses a suite of variables and parameters, outlined in Table 2.

First, the isostatic effect of any sediment deposited upon oceanic basement is accounted for by replacing it with an isostatically equivalent water load (Czarnota et al., 2013). This sedimentary correction, C_s, is given by

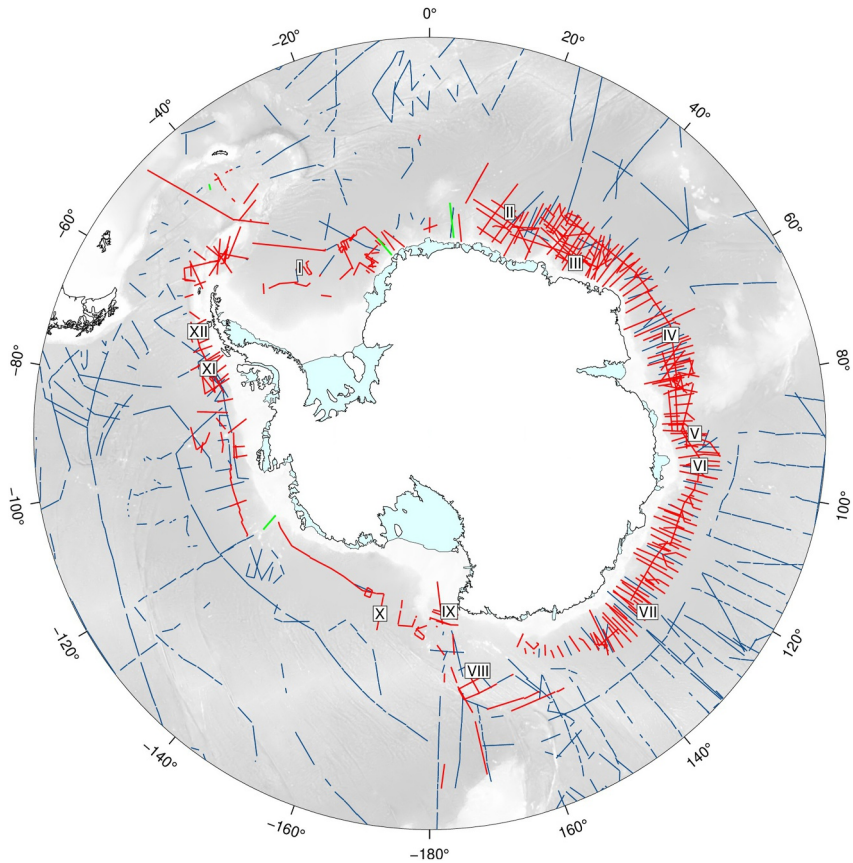

Figure 2. Seismic databases. Bathymetric map of Antarctica. White region = continental landmass as defined by grounding line; blue region = extent of ice shelves; blue lines = location of seismic experiments compiled by Holdt et al. (2022) including single and multi-channel reflection and wide-angle seismic experiments; red lines = 483 seismic reflection lines contributed by this study from SDLS (http://SDLS.ogs.trieste.it; Supporting Information S1); green lines = legacy wide-angle seismic experiments added in this study; white squares I–XII = location of seismic profiles presented in Figure 3.

$$C_s = \left(\frac{\rho_a - \overline{\rho}_s}{\rho_a - \rho_w}\right) z_s, \tag{1}$$

where the density of asthenosphere $\rho_a = 3.25$ Mg m^{-3} and the density of water $\rho_w = 1.03$ Mg m^{-3}. $\overline{\rho}_s$ and z_s are the average density and thickness of the sedimentary layer as interpreted from the seismic reflection data.

In order to define $\overline{\rho}_s$ and z_s, the observed thickness of the sedimentary column in TWTT, t, must be converted to depth, z, accounting for effects of compaction and composition on velocity. This relationship is defined empirically such that:

$$\frac{t}{2} = \frac{z}{v_{sg}} + \phi_\circ \lambda \left(\frac{1}{v_w} - \frac{1}{v_{sg}}\right)\left[1 - \exp\left(\frac{-z}{\lambda}\right)\right], \tag{2}$$

where the decay constant $\lambda = 2.3$ km, initial porosity $\phi_\circ = 0.67$, acoustic velocity of solid grains $v_{sg} = 4.50$ km s^{-1} and acoustic velocity of pore fluid $v_w = 1.5$ km s^{-1}. These parameters are defined using coincident seismic reflection and wide-angle experiments (Holdt et al., 2022). By using a compaction-based relationship, it then follows that the mean density of the sedimentary column, $\overline{\rho}_s$, relates to the thickness, z, such that:

$$\overline{\rho}_s(z) = \rho_{sg} + \frac{\phi_\circ \lambda}{z}(\rho_w - \rho_{sg})\left[1 - \exp\left(\frac{-z}{\lambda}\right)\right], \tag{3}$$

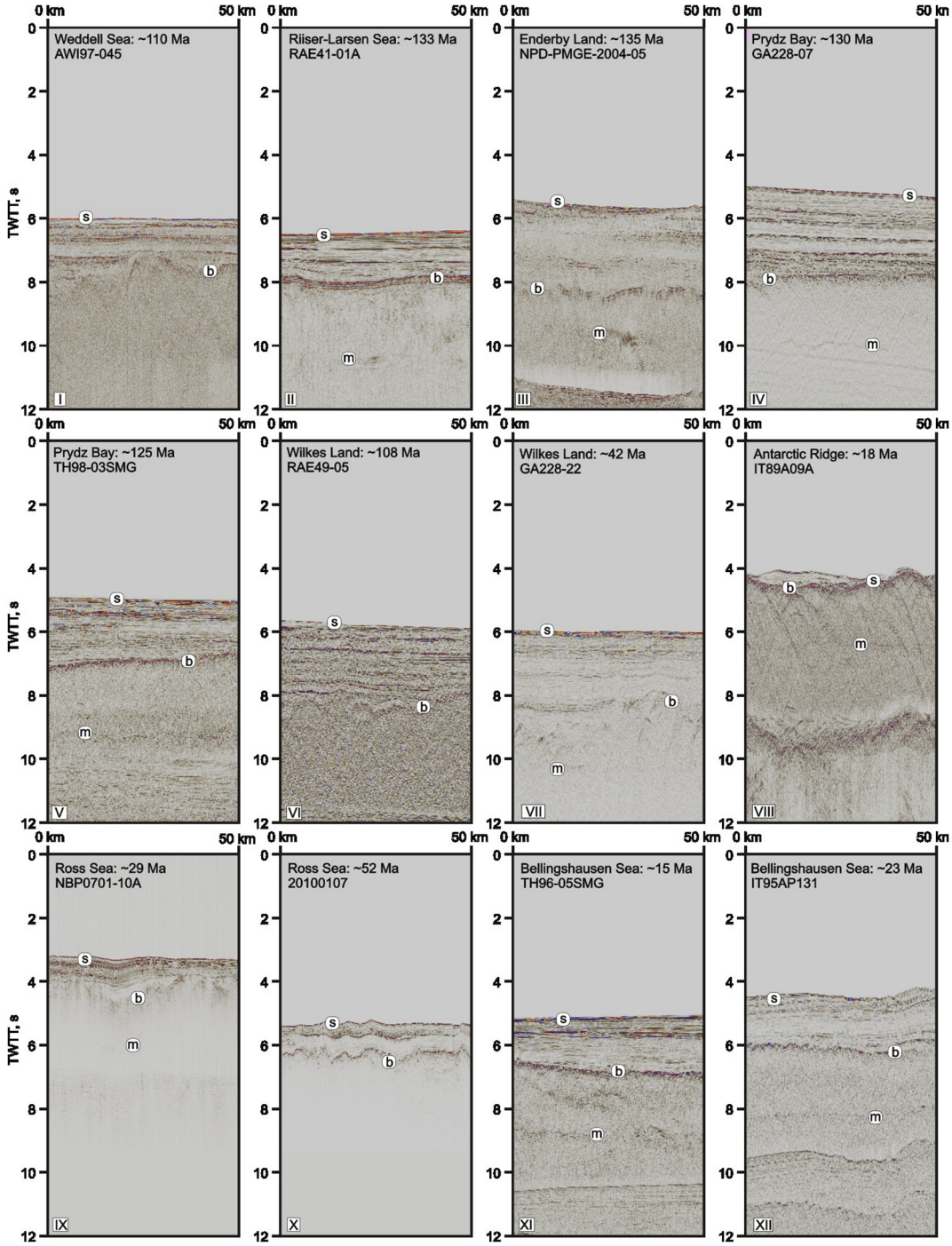

Figure 3. Multi-channel seismic (MCS) reflection images of oceanic crust. *s* = seabed; *b* = sediment-basement interface; *m* = basement-mantle interface; TWTT = two-way travel time. (I) MCS reflection profile of 110 Ma oceanic crust, Weddell Sea. (II) Riiser-Larsen Sea (133 Ma). (III) Enderby Land (135 Ma). (IV) Pyrdz Bay (130 Ma). (V) Pyrdz Bay (125 Ma). (VI) Wilkes Land (108 Ma). (VII) Wilkes Land (42 Ma). (VIII) Antarctic Ridge (18 Ma). (XI) Ross Sea (RS) (29 Ma). (X) RS (52 Ma). (XI) Antarctic Peninsula (23 Ma). (XII) Antarctic Peninsula (15 Ma). Note pronounced seabed multiples on several panels (e.g. III, VIII, XI, XII). Crustal ages taken from augmented version of Seton et al. (2020) global age grid (Figure 6). SEG-Y data from http://sdls.ogs.trieste.it.

Table 1
Additional Wide-Angle Seismic Experiments in Which Moho Refracted Phase, Pn, is Observed

Lines	Region	Reference
AWI20060200	Amundsen Sea	Lindeque et al. (2016)
I	Scotia Sea	Allen (1966)
96,100, 96,110	Lazarev Sea	Jokat et al. (2004)

where the solid grain density of quartz ρ_{sg} = 2.65 Mg m^{-3}, the density of seawater ρ_w = 1.03 Mg m^{-3} and λ and $\phi_\circ$ are the same as in Equation 2. Full methods can be found in Holdt et al. (2022).

Secondly, in instances where the Moho is identifiable, a crustal correction C_c, is applied to correct the water-loaded depth to basement for variations in the average crustal density, $\overline{\rho}_c$, and thickness, z_c, relative to the global average crustal density, $\overline{\rho}_r$, and thickness, $\overline{z}_r$, such that:

$$C_c = \left(\frac{\rho_a - \overline{\rho}_c}{\rho_a - \rho_w}\right) z_c - \left(\frac{\rho_a - \overline{\rho}_r}{\rho_a - \rho_w}\right) \overline{z}_r. \quad (4)$$

Reference crust has mean thickness $\overline{z}_r$ = 6.38 km, and mean density $\overline{\rho}_r$ = 2.84 Mg m^{-3}, and $\overline{\rho}_c$ and z_c are the measured density and thickness of the crustal layer, respectively (Holdt et al., 2022).

To convert seismic observations of the crust from TWTT to thickness a velocity conversion is required. For the crustal layer, this conversion is dependent on the thickness of the layer in time. Compositional changes associated with varying thickness of oceanic crust give rise to variations in average velocity with crustal thickness; for a given thickness in TWTT, there is a unique average velocity which can be used to convert from TWTT to thickness (See Figure 7 in Holdt et al. (2022)). Similarly, Carlson and Herrick (1990) have established a relationship, based on laboratory measurements, between the average p-wave velocity of oceanic crust and its density. By using these two empirical relationships, both $\overline{\rho}_c$ and z_c can be determined, defining the crustal correction, C_c, as a function of TWTT.

The majority of seismic profiles in the study did not permit a precise crustal correction to be calculated since no Moho reflection was evident in the MCS data. In a conciliatory attempt to account for the sparseness of crustal observations in Antarctica, crustal corrections contributed by this study, as well as from wide-angle seismic experiments in Holdt et al. (2022) were interpolated alongside their uncertainties between data points using a

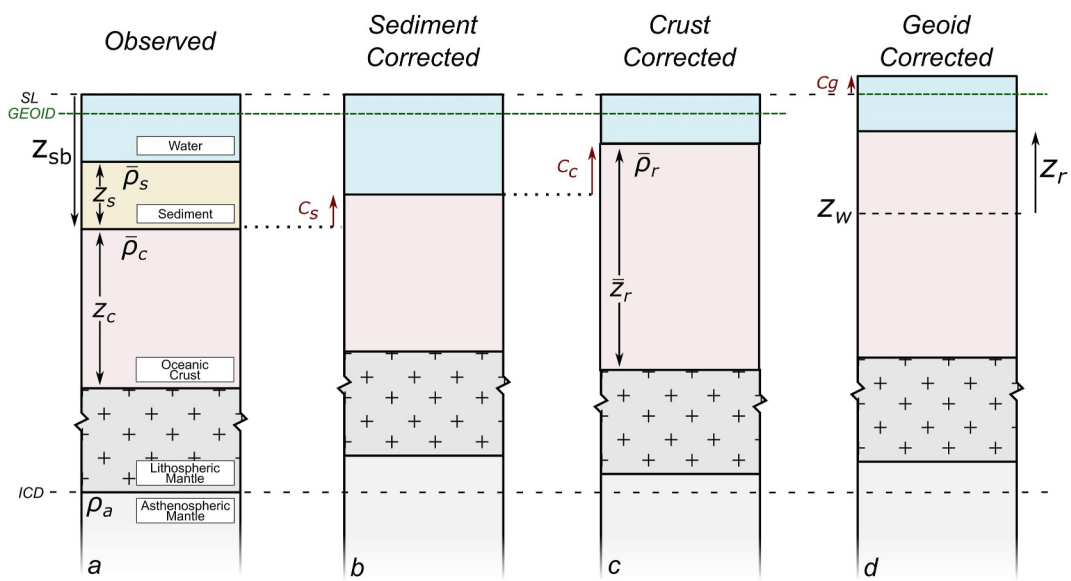

Figure 4. Corrections applied to seismic observations. (a) Observed column of oceanic crust. SL = mean sea level; ICD = isostatic compensation depth; z_sb = observed depth to basement; z_s = sedimentary thickness; z_c = crustal thickness; $\bar{\rho}_s$ = average sediment density; $\bar{\rho}_c$ = average crustal density; ρ_a = asthenospheric mantle density. Thicknesses and densities constrained from seismic data (Holdt et al., 2022). (b) Column where sediments have been replaced with isostatically equivalent water load through sediment correction, C_s. (c) Column where crustal heterogeneities in thickness and density have been accounted for, relative to global average crustal thickness, $\bar{z}_r$, and density, $\bar{\rho}_r$, through crustal correction, C_c. (d) Column where measurements defined relative to geoid through geoid correction, C_g. Residual depth, z_r, measured relative to expected water-loaded depth to basement, z_w, as determined from plate cooling model. Diagram not to scale.

Table 2
Symbols and Values of Parameters for Calculating Residual Depth/Topography

Symbol	Parameter	Value	Units
C_c	Correction due to oceanic crustal thickness	-	km
C_g	Correction due to geoid	-	km
C_s	Correction due to sedimentary load	-	km
λ	Compaction decay length	2.3	km
ϕ_o	Porosity, initial	0.67	dimensionless
$\overline{\rho}_c$	Density of oceanic crust (observed mean)	-	Mg m^{-3}
ρ_a	Density of asthenospheric mantle	3.25 ± 0.02	Mg m^{-3}
$\overline{\rho}_r$	Density of oceanic crust (global mean)	2.84 ± 0.07	Mg m^{-3}
$\overline{\rho}_s$	Density of local sediment (mean)	-	Mg m^{-3}
ρ_{sg}	Solid grain density	2.65 ± 0.05	Mg m^{-3}
ρ_w	Density of seawater	1.03 ± 0.01	Mg m^{-3}
t	Two-way travel time (TWTT)	-	s
$\overline{v}_p$	Average velocity of oceanic crust	-	km s^{-1}
v_{sg}	Acoustic velocity of solid grains	4.50 ± 0.50	km s^{-1}
v_w	Acoustic velocity of pore fluid	1.50 ± 0.01	km s^{-1}
z	Depth	-	km
z_c	Oceanic crustal thickness	-	km
z_o	Depth to water-loaded basement (observed)	-	km
z_r	Residual depth	-	km
$\overline{z}_r$	Oceanic crustal thickness (global mean)	6.38 ± 1.12	km
z_s	Sediment thickness	-	km
z_{sb}	Depth to seabed	-	km
z_w	Depth to water-loaded basement (expected)	-	km

tensioned biharmonic spline interpolation in GMT. A tension of 1 was used to produce a harmonic surface, ensuring that minima and maxima across the interpolation are only associated with data points and are not artificially inflated. Due to the high uncertainties of such an interpolation, this additional correction was only applied to seismic profiles within 500 km of definitive Moho (Figure 5).

For all measurements without a robust crustal correction, an indication of whether the consequent residual depth measurement should be considered a minimum/maximum constraint based on whether the crust is regionally thicker/thinner than average oceanic crust is provided symbolically. In this way, the symbols used throughout the following figures in this study uniquely highlight the highest quality observations in which both a sedimentary correction and a precise (i.e., not interpolated) crustal correction has been applied.

Once corrections to account for both sedimentary and crustal loading are defined, the water-loaded depth to basement, z_o, measured relative to the geoid is defined as:

$$z_o = z_{sb} + C_s + C_c + C_g, \tag{5}$$

where z_{sb} is the observed depth to the seabed and C_g is the height of the geoid. The geoid is an equipotential surface of Earth's gravity field that defines mean sea level and exhibits long-wavelength relief due to deep mantle density anomalies. Because bathymetric observations are referenced to mean sea level, applying this correction prevents long-wavelength geoid relief from being misinterpreted as residual bathymetry.

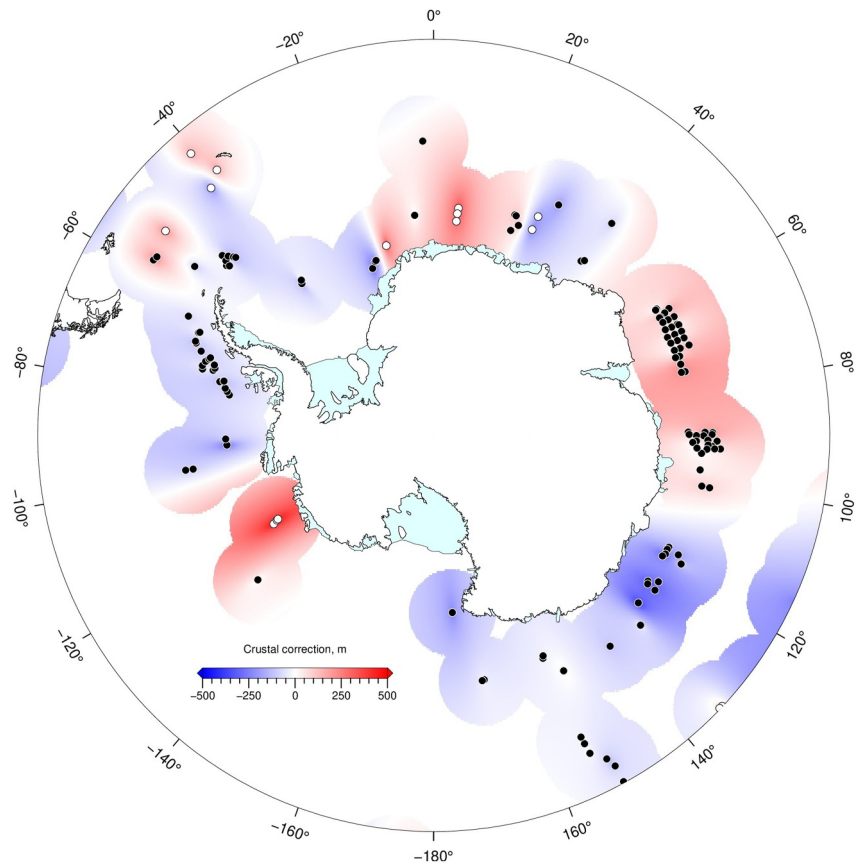

Figure 5. Southern Ocean crustal constraints. Crustal correction, C_c, interpolated up to 500 km from locations at which Moho was identifiable and used to correct measurements without crustal constraints. Black circles = location of crustal thickness observations from seismic reflection profiles, recorded in TWTT; white circles = location of crustal thickness observations from seismic wide-angle experiments, recorded in depth.

2.3. Global Plate Model and Age of Oceanic Crust

Having determined a water-loaded depth to basement, this value can then be compared to that predicted by a plate model. This study utilizes the revised plate model of Holdt et al. (2025). This global model is pressure and temperature dependent, produced by jointly inverting global water-loaded subsidence measurements and oceanic crust heat flow data. Observations globally fall within ±1.5 km of this plate model, as do the new measurements obtained in this study throughout Antarctica's fringing oceanic basins (Figure 6b).

In measuring residual depth relative to a plate model, the accuracy of any consequent dynamic topographic observations is intrinsically linked to the accuracy of the underpinning crustal age model. Figure 6a presents the age model which has been used in the study to determine the expected depth to basement and calculate residual depth anomalies. Initially, the Seton et al. (2020) age model was used. However, the resultant residual depth measurements highlighted regions in which the age of oceanic crust led to erroneous residual depths, deviating considerably from the typical ±1 km seen globally, most notably in the east-central SS (Figure 7).

The age of the east-central SS region is debated (Figure 7). Traditionally considered to be formed by rifting in a Miocene back-arc basin (Hill & Barker, 1980), Eagles (2010) inferred a Mesozoic age using heat-flow measurements, gravity and magnetic data. The interpretation of Eagles (2010) resolved a deficiency of the Hill and Barker (1980) interpretation; a spreading ridge which could have produced such young crust could not be identified (Livermore et al., 1994). However, residual depths calculated using this age imply up to 2.9 km of dynamic support which falls considerably outside of the expected range of ±1 km in global studies (Figure 7c). The crust would need to be between ~20–25 km thick to elicit a correction which would bring these observations in line with the global database. Such thick crust seems unlikely, especially given the result of legacy refraction

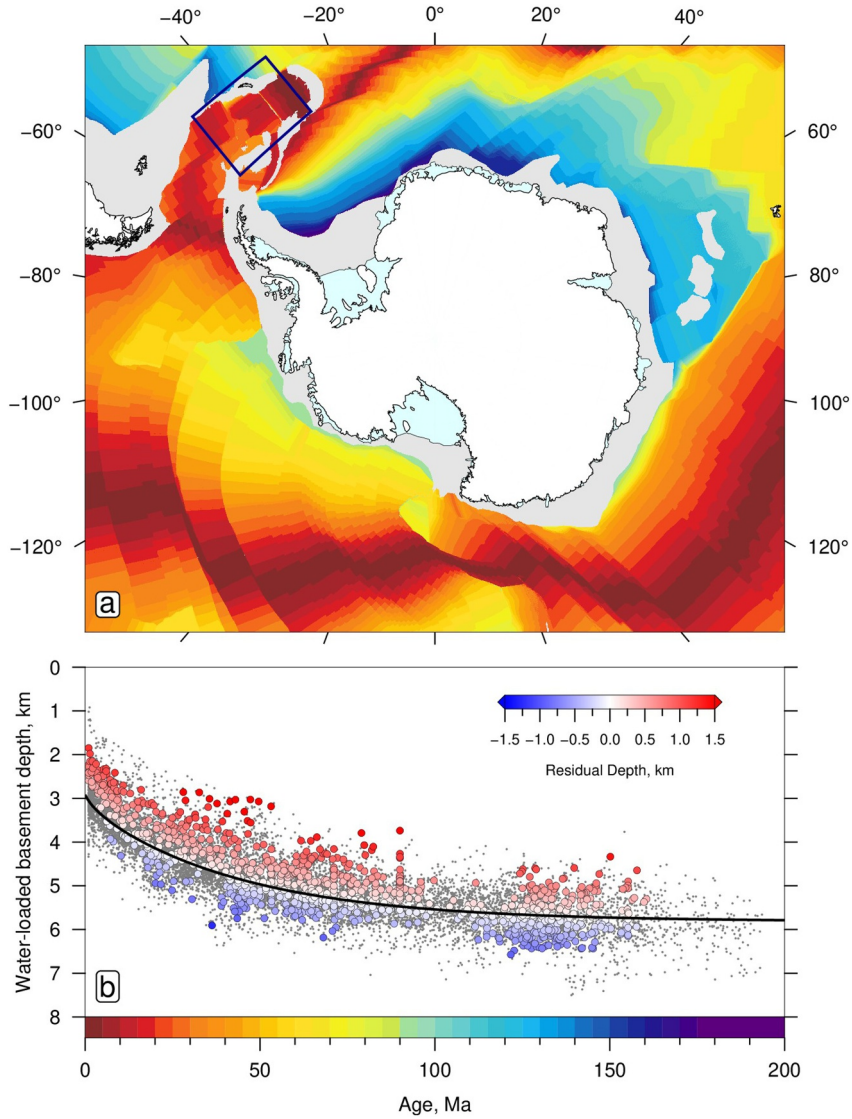

Figure 6. Age of oceanic crust. (a) Augmented crustal age model Seton et al. (2020), including updates to East Central Scotia Sea (Hill & Barker, 1980) and Bellingshausen and Amundsen Seas (Wobbe et al., 2012). Dark blue polygon = sub-region shown in Figure 7. (b) Plate model used to calculate residual depth from water-loaded depth to basement. Black line and gray dots = plate model against which residuals are measured and global age-depth inventory (Holdt et al., 2025); blue to red colored circles = age-depth measurements contributed by this study colored according to magnitude of residual depth anomaly.

experiments in the region which show the crust to be only 4.15 km thick (Allen, 1966). Similarly, wide-angle experiments south of South Georgia show the oceanic crust to be between 5 and 6.5 km thick (Allen, 1966; Ewing et al., 1971). Whilst both these experiments fall on the edges of the debated region, evidence for thick crust in the east-central SS is still lacking. Therefore, the only way to reconcile the observed water-loaded depth to basement measurements with global observations is to return to the interpretation of Hill and Barker (1980), but fundamental questions regarding the origin of this young crust remain.

Minor adjustments were also made to the continent-ocean boundary and oldest crust in the Amundsen Sea. Whilst of minimal consequence to the residual depth anomalies, this update reflects revised magnetic anomalies used by Wobbe et al. (2012) to constrain the rifting of West Antarctica from Zealandia which were not included in the Seton et al. (2020) compilation. Similarly, in the Macquarie region, the transtensional fracture zone offsetting the Pacific-Antarctic ridge appears to have been oversimplified in the Seton et al. (2020) compilation. To rectify this

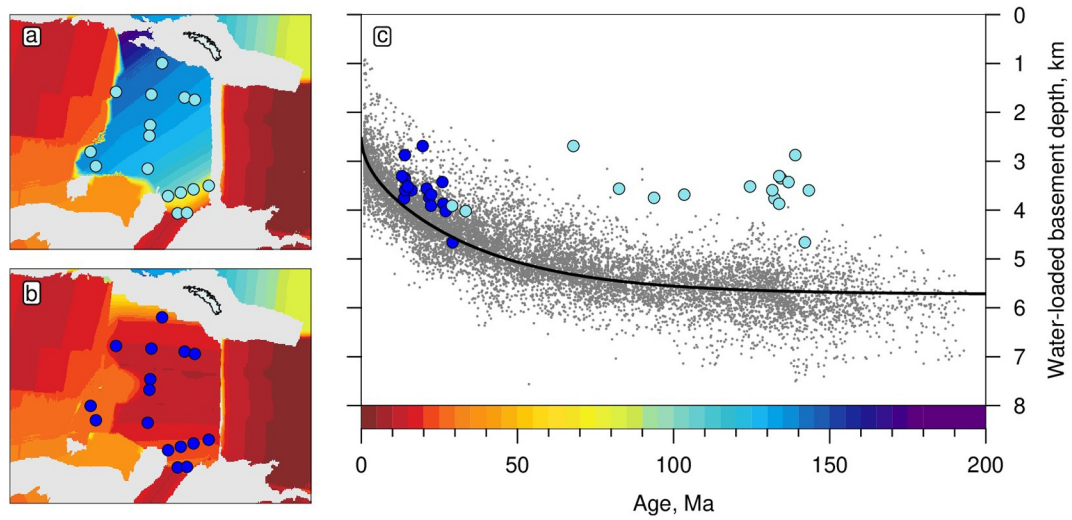

Figure 7. Alternative age models for East Central Scotia Sea (SS). (a) Crustal age in East Central SS as presented in Seton et al. (2020), based on heat flow measurements (Eagles, 2010). Light blue circles = location of spot measurements in panel (c). (b) Crustal age based on magnetic anomalies interpreted by Hill and Barker (1980) used throughout this study. Dark blue circles = location of spot measurements in panel (c). (c) Effect of changing crustal age on age-depth measurements. Black line = plate model against which residuals are measured; light gray circles = global scatter of age-depth inventory; light blue circles = age-depth measurements based on sea floor ages depicted in panel (a); dark blue circles = age-depth measurements based on sea floor ages depicted in panel (b).

issue, the Seton et al. (2020) model is replaced with an interpretation from Croon et al. (2008) and Eagles et al. (2009) to reflect the young spreading seen in magnetic data along this section of the ridge. This change makes residual depth measurements in the region consistent with the amplitude range seen both throughout the Southern Ocean and globally.

It is important to consider that this age-dependent correction only accounts for the expected effects of lithospheric thickening as a function of plate age. No direct observations of lithospheric thickness were made or corrected for. In this way, small-scale deviations in lithospheric thickness caused by temperature anomalies at the base of the lithosphere can still exert a buoyancy effect on the bathymetry which is therefore included in the residual bathymetric signal.

2.4. Results

Upon binning observations made along 483 additional seismic reflection lines into intervals of 1°, the SDLS archive has provided 780 further spot measurements of residual depth, bringing the total number south of −50° to 2,105. In the Southern Ocean specifically (south of −60°), there has been an almost three-fold increase in the number of measurements to 1,120 when compared to Holdt et al. (2022), thus greatly improving density of coverage in proximal Antarctic oceanic regions (Figure 8a, Data set S2).

Despite improved coverage, there is still an uneven distribution of measurements across the Southern Ocean. It is therefore commonplace to fit a spherical harmonic representation to produce a smoothed and damped representation of the data. Residual topography and bathymetry measurements have been historically used to obtain such spherical harmonic representations of dynamic support (e.g., Hoggard et al. (2017); Holdt et al. (2022)), allowing for evaluation of the power spectra, the shape of which has consequences for our understanding of mantle flow. Holdt et al. (2022) demonstrated that a power spectrum, which peaks at spherical harmonic degree $l = 2$ with power out to and including $l = 40$, can be robustly recovered from global residual spot measurements. This spectrum suggests a lower bound for convection-related topography of $\lambda \approx 10^3$ km and the spectral slope shows that the power of dynamic topography decreases with increasing wavelength as a function of k^{-1}. This slope is a manifestation of pink noise, and is analytically consistent with mantle convection as the product of Stokes' flow (viscous, laminar) as opposed to more turbulent or plate-driven flow which would exhibit different gradients across the power spectrum (Hoggard et al., 2017; Holdt et al., 2022).

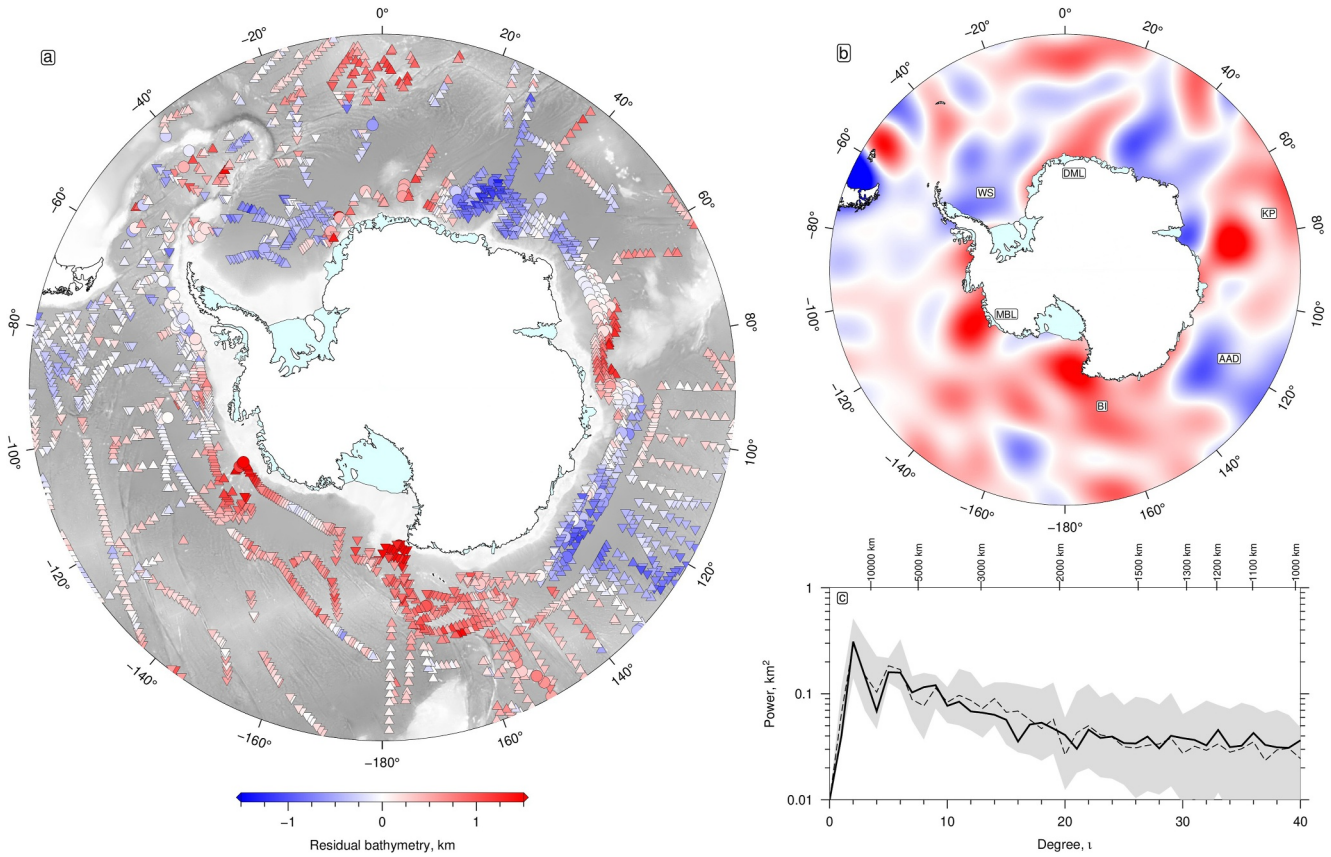

Figure 8. Antarctic map of residual depth and spherical harmonic representation. (a) Colored circles/triangles = residual depth measurements averaged over 1° bins. Circles = measurements with both sediment and crustal corrections applied; downward/upward pointing triangles = measurements that are upper/lower limits with only sedimentary corrections as inferred from regional crustal constraints. Triangles within 500 km of crustal constraint have had crustal correction applied (Figure 5) but are still represented by triangles due to inherent uncertainty in regional correction. (b) Spherical harmonic representation of residual bathymetry calculated using regularized least-squares inversion of Hoggard et al. (2016) global database and additional Southern Ocean data out to, and including, degree $l = 40$. WS = Weddell Sea; MBL = Marie Byrd Land; Dronning Maud Land = Dronning Maud Laud; BI = Balleny Islands; AAD = Australia-Antarctic Discordance; KP = Kerguelen Plateau. (c) Power spectrum. Bold line with gray band = power spectrum and uncertainties estimated from range of gradient regularization and amplitude damping coefficients ($10^{0.5}$–$10^{+0.5}$ and 102–103, respectively) for the global database augmented with data from this study; dashed black line = power spectrum from Holdt et al. (2022).

Following this approach, we use the regularized least-squares inversion of Hoggard et al. (2016) to update the global spherical harmonic representation of dynamic topography, combining the new Antarctic data with the oceanic database of Holdt et al. (2022) and the continental database of Stephenson et al. (2024) (Figure 8b). The additional measurements provided by this study better constrain the spatial distribution of dynamic swells in the Antarctic, but result in little change to the power spectrum compared to that of Holdt et al. (2022). There remains considerable power out to and including spherical harmonic degree $l = 40$, beyond which point it may become challenging to disentangle dynamic topographic signals from flexural loading, or discern it given the uncertainty in the data (Figure 8c).

Regions of notable dynamic support up to 1 km include south of the Kerguelen Plateau (KP), the Marie Byrd Seamounts, the Ballenny Islands, and offshore DML. The Weddell Sea and Australia-Antarctic Discordance (AAD) make up major regions of negative residual bathymetric observations.

3. Relation of Residual Depth Measurements to Other Observations

3.1. Free-Air Gravity Anomalies

It has long been recognized that dynamic topography can be inferred from geoid and gravity anomalies due to the causal density anomalies which induce vertical plate motion (Hager & Richards, 1989; Panasyuk & Hager, 2000). Admittance is the proportionality between gravity anomalies and surface topography, quantifying how subsurface

density structure is expressed within the observed gravitational field. More specifically, the scaling between long-wavelength free-air gravity anomalies and known dynamic topographic anomalies has defined the oceanic admittance value, $Z = 30$ mgal km^{-1}, which is used to predict dynamic topography in the absence of direct observations (Crosby et al., 2006; Hoggard et al., 2016; Winterbourne et al., 2009). This relationship is predicated on the long wavelength gravity field being insensitive to shallow density anomalies that affect isostatic topography, and instead reflects deeper density anomalies in the mantle which drive dynamic support. This augmented Antarctic data set provides new opportunities to gauge the applicability of using admittance as a predictive tool for dynamic topography.

Scaling of the long-wavelength ($\lambda > 730$ km) free-air anomaly by an admittance of $Z = 30$ mgal km^{-1} results in predictions which can deviate considerably from residual depth observations (see Hoggard et al. (2017)). For residual depth measurements in the Southern Ocean, the Pearson correlation coefficient with the free-air anomaly stands at only $r = 0.28$. These discrepancies can be mostly attributed to the depths to which gravity fields and topography are sensitive. Surface response kernels and tomographic correlations suggest that the majority of dynamic topography is generated by upper mantle anomalies shallower than 500 km, whereas gravity observations are sensitive down to the lower mantle (Holdt et al., 2022; Richards et al., 2018). The differences between the observational data set and gravity-derived predictions can therefore be accounted for, owing to the different regions of the mantle sampled.

In this study, we test whether it is possible to improve the correlation between the free-air gravity anomaly and residual depth measurements through bandpass filtering of the gravity anomaly (Figure 9). We sweep through a series of upper and lower spherical harmonic bandpass filter limits for the gravitational field and calculate the Pearson correlation coefficient, r, between the filtered free-air gravity anomaly and the spherical harmonic representation ($l = 40$) of dynamic topography, only at the location of spot measurements (Figure 9). The correlation is greatest when removing spherical harmonic degrees $l < 12$ and $l > 29$ from the free-air gravity anomaly, despite the spherical harmonic model of residual bathymetry being composed of all degrees out to and including $l = 40$ (Figure 9a). Removing the longer wavelength/low spherical harmonic degree components of the field significantly improves the spatial correlation, whereas the maximum spherical harmonic degree has negligible effect on the correlation, especially beyond $l = 35$. This trend implies that the gravity signal at shorter wavelengths is beginning to be contaminated by crustal and ice signals which are not reflected in the residual depth spot measurements and the correlation is therefore insensitive to these wavelengths. Assuming a very simplified relationship between the wavelength of an anomaly and the causative body, such that the depth is approximately half the wavelength, density anomalies deeper than ≈ 530 km need to be filtered from the gravity signal to most improve the correlation (Bowin et al., 1986). Whilst this relationship only serves as a rough estimate of the depth of causative anomalies, the observation is consistent with response kernel studies which show dynamic topography to be most sensitive to the upper mantle, especially on shorter wavelengths (Holdt et al., 2022; Richards et al., 2018).

The improved co-location of free-air gravity anomalies and residual depth anomalies provides a more reliable insight into potential support in the continental realm (Figure 9c). Notably, the positive increase in residual depth anomalies moving south from the AAD toward the continent is reflected in the positive filtered free-air gravity anomalies along the coastline. The MBL anomaly also continues significantly further inland when the longest wavelengths are filtered from the gravity data, implying greater dynamic support beneath the West Antarctic Rift System (WARS) compared to interpretations drawn purely from the non-hydrostatic anomaly (see Figure 1b). However, there still remain regions of significant divergence between the two data sets (Figure 9d), consistent with other observations that notable dynamic topography can exist in the absence of a corresponding free-air gravity anomaly, and that a single admittance value cannot capture the complexity of dynamic mantle support on regional scales (Colli et al., 2016). Such observations highlight the importance of using direct observations of the crust rather than relying on potential field data when quantifying dynamic support and gauging upper mantle convective patterns.

3.2. Residual Shear-Wave Tomography

Further assessment of the relationship between residual depth and geodynamic mantle processes can be gained through considering results in light of surface-wave tomographic models. In the same way that the bathymetry of the oceans varies as a function of plate age, velocity anomalies in the upper mantle are dominated by lithospheric cooling, masking anomalies which contribute to sub-plate buoyancy. By stripping out this cooling signal from

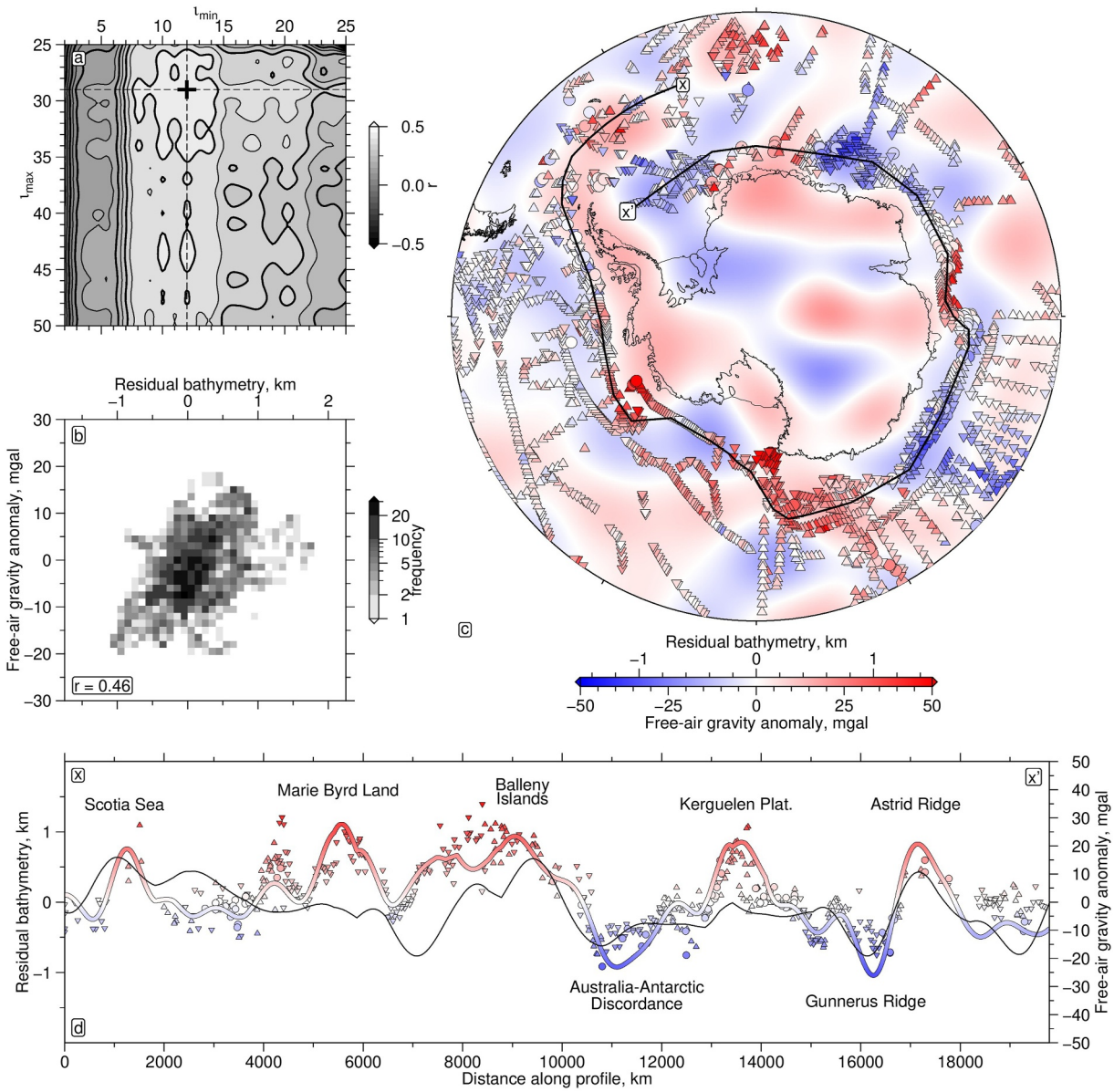

Figure 9. Correlation between residual depth and free-air gravity anomalies. (a) Pearson's correlation coefficient, *r*, between spherical harmonic representation of residual depth, (at locations of spot measurements) and free-air gravity anomaly bandpass filtered. Dashed lines and cross mark best correlating combination of $l_{min} = 12$ and $l_{max} = 29$ for filtering. (b) Cross plot showing correlation between optimal bandpass filtered free-air gravity anomaly and residual depth. (c) Optimal bandpass filtered ($\lambda \approx 3300$–1,400 km) free-air gravity anomaly. Colored circles/triangles = residual depth measurements as in Figure 8; black line = transect shown in (d). (d) Transect from x - x'. Colored circles/triangles = residual depth measurements within 100 km of transect; colored band = spherical harmonic representation of residual depth out to and including degree $l = 40$; black line = free-air gravity anomaly as in panel (c).

tomographic models, Richards, Hoggard, Crosby et al. (2020) identified a correlation between positive residual depth anomalies and slow shear wave velocity anomalies within the upper 400 km of the Earth's mantle on a global scale. The revised residual depth database and resultant spherical harmonic model presented here provide new opportunities to assess the correlation between residual depths and seismic velocity anomalies in the Southern Ocean.

The shortage of permanent seismic stations in Antarctica and surrounding regions limits available broadband seismic data for tomographic imaging. However, incorporating recent temporary deployments across East and West Antarctica, Lloyd et al. (2020) developed a continental-scale adjoint tomographic model of upper mantle shear-wave velocity. By including surface-wave data they were able to image small-scale anomalies associated

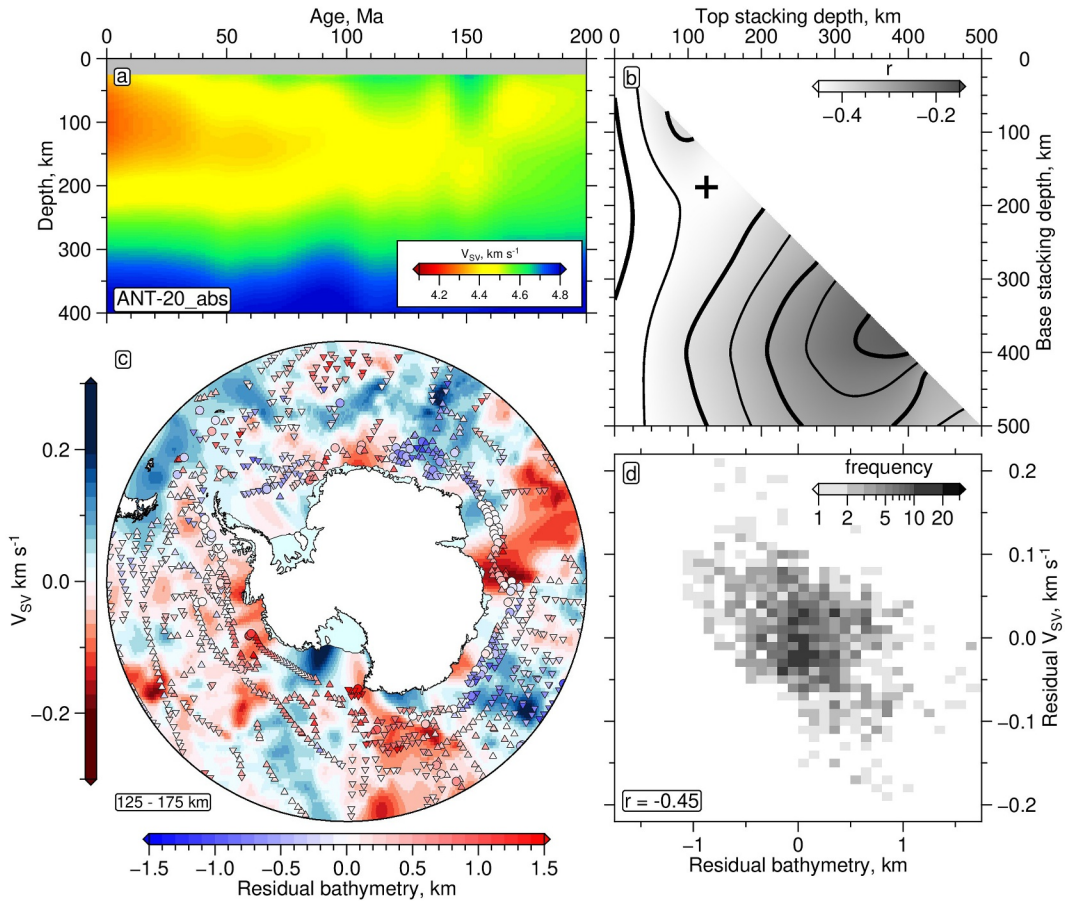

Figure 10. Correlation between residual depth and residual tomographic models. (a) Relationship between age, depth and shear-wave velocity for ANT-20 tomographic model for the Southern Ocean (Lloyd et al., 2020). (b) For varying stacking intervals, Pearson's correlation coefficient, *r*, between spherical harmonic representation of residual depth (at locations of spot measurements) and residual shear-wave velocities. Residual velocities calculated by stripping relationship in (a) from ANT-20, based on age grid in Figure 6. (c) Residual tomographic model averaged over optimal stacking depth 125–175 km as determined in (b). Colored circles/triangles = residual depth measurements as in Figure 8 in 2° bins. (d) Cross plot showing correlation between residual shear-wave velocity and residual depth for optimal stacking window.

with advection beneath Antarctica for the first time, making it the most appropriate model to use in assessing the extent to which upper mantle anomalies contribute to dynamic topography. We also consider global models, namely SL2013 and CAM2016 (Ho et al., 2016; Schaeffer & Lebedev, 2013), which image mantle velocity anomalies at lower resolutions than regional models but have been shown to correlate reasonably well with dynamic topography elsewhere (Richards, Hoggard, Crosby et al., 2020).

Anomalies associated with convective flow are isolated by removing the component of absolute velocity associated with plate cooling, following the method of Richards, Hoggard, Crosby et al. (2020). Anomalous regions are first excised from the data, including major fracture zones, seamounts and large igneous provinces, as defined by Hoggard et al. (2017). Velocity data are then stacked as a function of depth and plate age into 2 Myr bins, using the revised age model (Figure 10a). This method allows for an average velocity to be calculated for any given age/depth and subtracted from the observed velocity. This residual velocity is therefore independent from all effects of plate cooling, making it more comparable with residual depth measurements which have also had the effects of plate cooling stripped.

To ascertain which mantle depths contribute most to dynamic support, for a given residual model, tomographic slices are stacked and averaged across a suite of top and base stacking depths at 5 km intervals. Both the stacked grids and the spherical harmonic representation of residual depths, up to and including spherical harmonic degree $l = 40$, are sampled point-wise at locations where spot measurements of residual depth have been defined. A

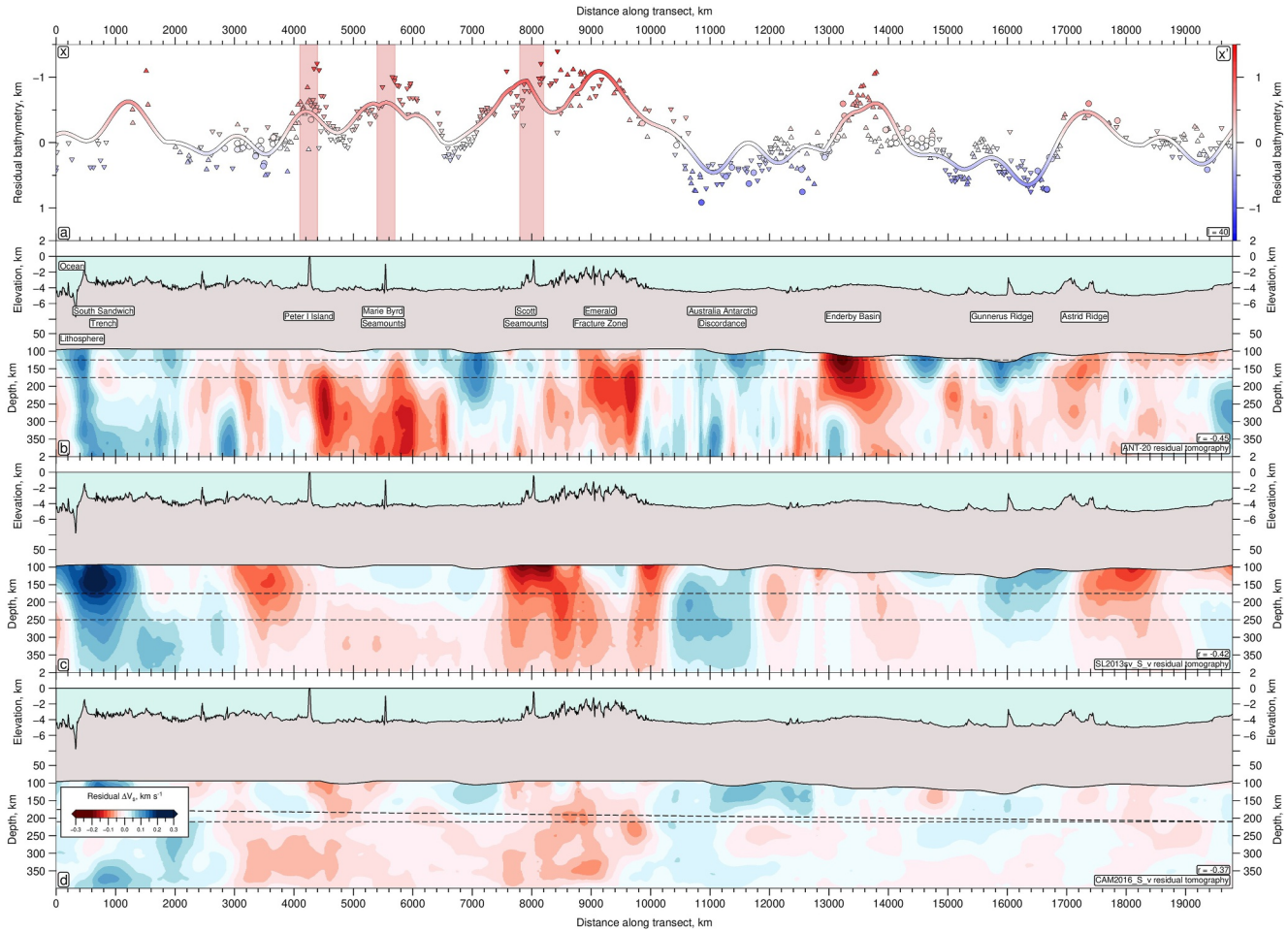

Figure 11. Circum-Antarctic transects showcasing residual tomographic anomalies. Transect from x–x' as in Figure 9. (a) Colored circles/triangles = residual depth measurements as in Figure 8 within 100 km of transect; colored band = spherical harmonic representation of residual depth out to and including degree $l = 40$; red bands = regions of Neogene intraplate basaltic volcanism. (b) Residual shear-wave velocity for ANT-20 (Lloyd et al., 2020). Gray = oceanic lithosphere as defined by F. Richards, Hoggard, White, and Ghelichkhan (2020); dashed lines = upper and lower stacking depths used to obtain best correlation between residual velocity and residual depth. For 125–175 km, $r = -0.45$. (c) Same for SL2013 (Schaeffer & Lebedev, 2013). For 175–250 km, $r = -0.42$. (d) Same for CAM2016 (Ho et al., 2016). For 170–210 km, $r = -0.37$.

Pearson correlation coefficient, r, between the two data sets is then calculated to determine the mantle depth range most greatly influencing bathymetry.

Figure 10b shows how the r value varies as a function of the stacking interval depth range. For ANT-20, the best statistical correlation with residual depth is achieved with tomographic slices averaged between 125 and 175 km ($r = -0.45$). The residual shear-wave anomaly for this interval is shown in Figure 10c and the extent of the correlation is highlighted by the crossplot in Figure 10d. This distribution suggests that all of the upper asthenosphere is contributing toward supporting oceanic bathymetry.

Residual tomographic anomalies are also calculated for the two global models, SL2013 and CAM2016. As with ANT-20, SL2013 shows correlations throughout the upper mantle, down to depths of 350 km with the best correlation window at 175–250 km ($r = -0.42$). CAM2016 shows a much poorer affinity to residual depth measurements, though again the best stacking interval is within the upper mantle at 170–210 km ($r = -0.37$). The residual tomographic anomalies are visualized on a circum-Antarctic transect, highlighting the best correlating depth windows (Figure 11).

Positive dynamic swells coincident with Neogene volcanism along the transect peak at +1 km and are centered on Peter I Island, the Marie Byrd seamounts, and the Scott Seamounts (Figure 11). Neogene volcanism at Peter I Island and the Scott Seamounts is consistently underlain by slow residual shear-wave velocity anomalies. The

extent of mantle anomalies beneath the Marie Byrd Seamounts is less robust, with no major tomographic anomaly evident in SL2013 (Figure 11c). However, the ANT-20 model, with improved horizontal resolution, shows a clear anomaly in this region (Figure 11b). Rifting initiated in this region ~90 Ma but $^{40}Ar/^{39}Ar$ ages of 65–56 Ma for the majority of the Marie Byrd Seamounts indicate formation significantly postdates ridge formation (Kipf et al., 2014). Cenozoic volcanism has also been identified at Peter I Island (0.1–0.35 Ma (Prestvik et al., 1990); 1.8 Ma (Kipf et al., 2014)) and one Marie Byrd Seamount (3.0 Ma (Kipf et al., 2014)), showing distinct phases of intraplate magmatism. There is no indication of an age-progressive spatial trend as typically characteristic of mantle plumes. Given that the Antarctic plate has been relatively stationary throughout the period of volcanism, as determined in hotspot reference frames and from plate kinematic reconstructions (Eagles et al., 2004; Wobbe et al., 2012), a plume origin cannot be ruled out. Alternatively, volcanism could also result from continental insulation flow (Kipf et al., 2014). Collectively, the coincidence of residual depth and tomographic anomalies with intraplate volcanism supports an upper mantle origin for dynamic support, though the source of this warm material specifically remains to be determined.

Other major peaks in residual depths are over the Enderby basin, south of the KP, and the Astrid Ridge (AR) (Figure 11). Break up of India and Antarctica ~133 Ma initially began with magma-poor rifting, resulting in thin crust close to the continental margin. This was followed by impingement of the Kerguelen plume and extrusion of a large igneous province with thicker oceanic crust, leading to the formation of the KP (Frey et al., 2000). Even after accounting for these observed variations in crustal thickness, there remain substantial residual depth anomalies of up to +1 km in Enderby Basin. The lack of causative anomalies for these observations in the SL2013 and CAM2016 models (Figures 11c and 11d) would suggest that dynamic support in this region may be dominated by lithospheric thinning rather than asthenospheric upwelling, though there is a major slow residual shear-wave velocity anomaly seen in the ANT-20 model (Figure 11b). The AR similarly formed during the break up of Gondwana. Wide-angle experiments in the region suggest rifting resulted in significant magmatic underplating and volcanic provinces in the region which could account for the +600 m residual depth anomalies (Jokat et al., 2004; Siddiquie et al., 1988). There is also evidence for more recent uplift, based on fault scarps cross-cutting the youngest sediments deposited in the region (Siddiquie et al., 2006). Such uplift can be accounted for by the slow residual velocity anomalies seen throughout tomographic models.

The two major regions of negative residual depths, up to −1 km, are at the AAD and the Gunnerus Ridge (GR) (Figure 11). The AAD is considered to be the product of downward mantle flow which has resulted in low mantle temperatures and reduced melting at the south-eastern section of the Indian Ridge (Sempeéreé et al., 1991). This has been challenged by Gurnis and Muller (2003) since global shear-wave models do not exhibit fast velocity anomalies. However, stripping out the velocity anomaly associated with the relatively young plate age in this region shows that the residual tomographic anomaly is broadly consistent with the negative residual measurements. Likewise, the dual-domal residual depth draw downs straddling the GR are mirrored in the fast residual tomographic anomalies in ANT-20 and SL2013 and a laterally smeared anomaly in CAM2016, supporting an upper mantle origin for the residual depth anomalies (Figure 11).

Despite broad similarities, no tomographic model produces a correlation coefficient with residual depth measurements exceeding $r = -0.45$, and none are capable of spatially reproducing all of the dynamic swells posited by these measurements. As with the free-air gravity anomaly, such discrepancies, as well as a lack of consistency between different tomographic models, highlights the importance of residual depth observations.

3.3. Neogene Intraplate Volcanism

The relative age of continents in comparison with the oceans means continental lithospheric architecture is considerably more complex, with greater variation in thermo-chemical composition due to depletion within the lithosphere (Jordan, 1975). This complexity, along with uncertainties associated with accounting for ice sheet loading, leads to higher uncertainty in calculating and correcting for isostatic contributions to Antarctica's continental topography. Furthermore, models of crustal thickness throughout Antarctica diverge considerably depending on both the specific data sets and methods used to define the Moho. Consequently, existing models of residual elevation show considerable differences throughout both East and West Antarctica (Pappa et al., 2019; Paxman, 2023). Offshore and onshore anomalies globally, however, are largely contiguous, meaning the new oceanic database can be exploited to provide spatial context to onshore studies against which continental observations can be considered (Stephenson et al., 2024).

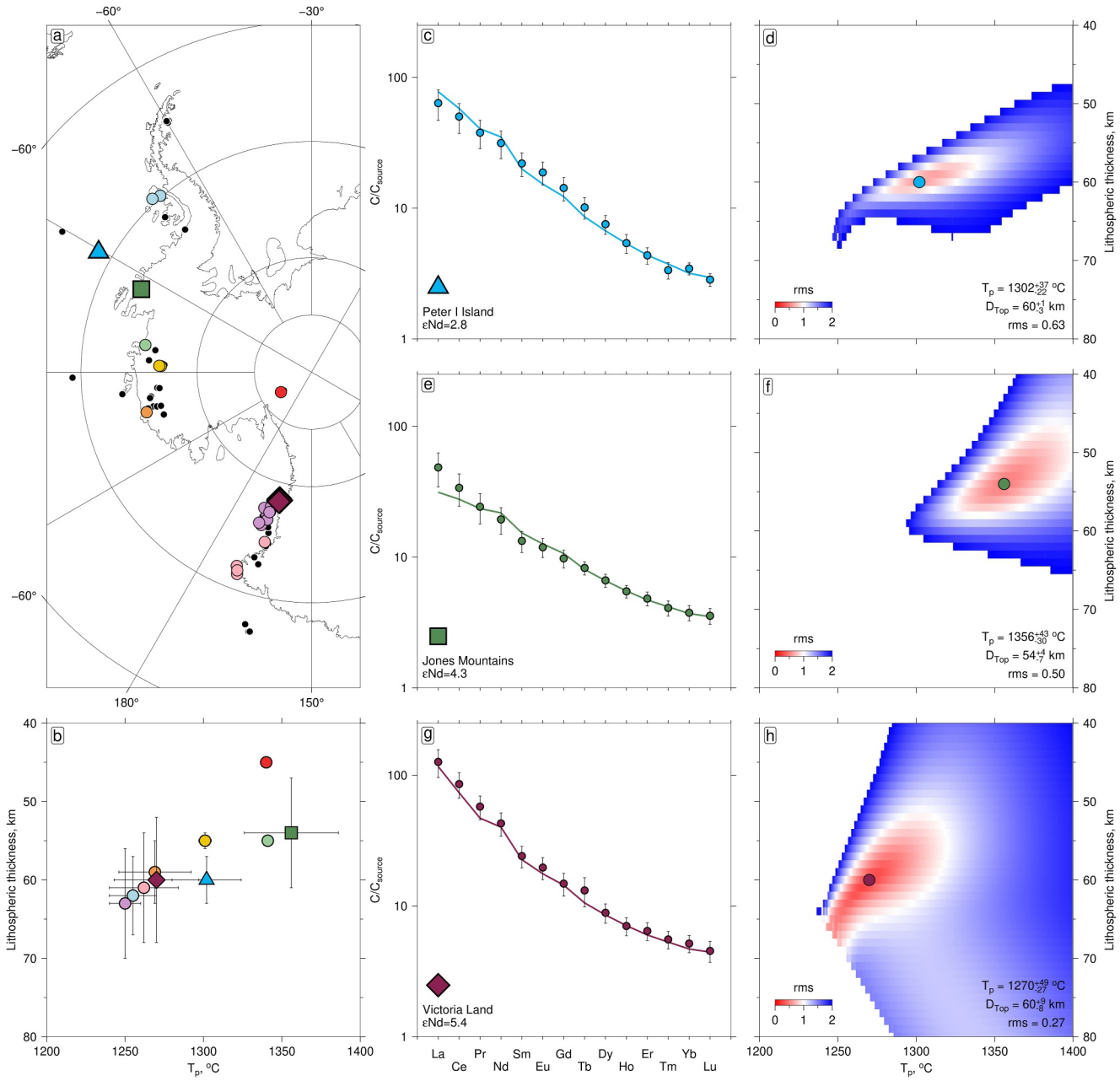

Figure 12. Inverse modeling of rare earth element (REE) concentrations in intraplate Neogene basalts. (a) Black circles = location of intraplate Neogene basalt samples; colored circles = samples which fit the criteria for REE modeling; large colored symbols = examples highlighted in (c–h). (b) Lithospheric thickness and temperatures determined from REE modeling with associated errors. Colors as in (a). Horizontal and vertical bars define limits at 1.5 × rms of global minimum. (c) Peter I Island. Circles with vertical bars = average REE concentration $\pm\sigma$ normalized with respect to source composition, defined according to εNd; colored line = REE concentrations calculated for best fitting lithospheric thickness and mantle potential temperature. (d) Misfit between modeled and observed REE concentrations as a function of lithospheric thickness and mantle potential temperature. Colored circle = locus of global minimum. (e–f) Jones Mountains (Marie Byrd Land). (g–h) Victoria Land (northern Transantarctic Mountains).

We therefore use volcanism to assess the continuity of dynamic swells evident in the oceanic realm beneath the Antarctic Ice Sheet. The spatial distribution of Neogene intraplate volcanism is known to be coincident with slow shear-wave velocity anomalies, thin lithosphere, and regions of positive dynamic topography (Ball et al., 2021). In Antarctica, we augment the global database of Ball et al. (2021) to ascertain the known distribution of intraplate volcanism across western Antarctica (Data set S1, Figure 12a). There are three main clusters of continental volcanism; MBL, the Antarctic Peninsula and the TAM.

Basaltic rock compositions allow for further interrogation of the lithosphere and asthenosphere in these regions. REE concentrations of basaltic rocks record melting history from mantle source to eruption. Specifically, they vary with the mantle source composition and the melt fraction as a function of depth to the base of the lithosphere. This dependency can be used to model REE concentrations and constrain estimates of the depth to the top of the melt column, D_{top} (i.e., lithospheric thickness), and mantle potential temperature, T_p, for basalt samples acquired across Antarctica.

In order to model the REE distribution of a melt, it is necessary to make simplifying assumptions regarding the mantle source composition. We model a uniform lherzolitic source, with the extent of depletion varying linearly between primitive mantle and depleted mid-ocean ridge basalt mantle as a function of εNd (i.e., the deviation in the ratio of stable to radiogenic neodymium isotopes from a standard chondritic meteorite sample). Melting parameterization follows the hydrous melting model of Katz et al. (2003). Necessarily, the weight fraction of water in the source, $X^{bulk}_{H_2O}$, is defined such that $X^{bulk}_{H_2O}/X^{bulk}_{Ce} = 200$. The depth to spinel-garnet transition zone also influences the REE concentrations. We define this zone to be between 63–72 km (Jennings & Holland, 2015).

Following the framework of Ball et al. (2021), we perform a systematic grid sweep varying D_{top} and T_p values from 40–80 km and 1,200–1400°C, respectively. The `INVMEL-v12` geochemical model is used, assuming adiabatic melt paths, to model the REE distribution within the melt phase (McKenzie & O'Nions, 1991). The root-mean-square (rms) misfit between the observed and modeled REE concentrations, both normalized against source composition, is then calculated. The global minimum of rms misfit is considered to be the most likely parameter combination, but there is an inherent trade-off between lithospheric thickness and mantle potential temperature.

REE element modeling is applied in this way to Data set S1. To ensure that melts have not undergone significant fractional crystallization or olivine accumulation, we limit the database to only include samples with an MgO content between 9 and 15 wt% and correct observations for olivine fractional crystallization (Ball et al., 2021). The database is further filtered to ensure modeling is only carried out when >7 REE concentrations are recorded to ensure the rms misfit is statistically significant. Previous studies have also use the `MORVEL` plate motion model to remove samples which have moved >1000 km since eruption, but the relative stability of the Antarctic plate means this has no impact on our database (DeMets et al., 2010). Samples meeting these criteria ($n = 118$) were grouped into 10 provinces based on location (Figure 12a), with the consequent REE modeling results summarized in Figure 12b. Specific examples of how modeled REE distributions compare to the observed data are shown in Figures 12c–12h.

As expected for a thermal boundary, there is a relative relationship between lithospheric thickness and mantle potential temperature; thinner lithosphere is on average associated with higher potential temperatures. The lithospheric thicknesses of all groups are consistently thin, between 40–65 km. Mantle potential temperatures, however, are on average below that of ambient mantle (1312°C for our melt parameterization). Cooler temperatures are most prominent in the Antarctic Peninsula and Victoria Land regions. In Victoria Land, subduction along the Palaeo-Pacific margin contributed to the formation of pyroxenite, which has been incorporated into Cenozoic melts as shown by the presence of pyroxenite xenoliths (Martin et al., 2015). Recent trace element analysis of olivines from the Antarctic Peninsula by M. J. Hole et al. (2023) similarly point to a pyroxenite-dominant source. This source is potentially derived from delaminated continental lithosphere and sampled by magmatism due to the opening of a slab window following subduction of the Phoenix Ridge, allowing magmatism to originate from beneath the slab itself. For both these localities, using a pure lherzolite source to model mantle melting that includes a pyroxenite component will result in an underestimation of mantle potential temperature, accounting for the low modeled values of T_p, seemingly anomalous to regions of active mantle upwelling (Matthews et al., 2021).

By integrating these REE modeling results with additional data sets, we can ascertain the spatial variability in dynamic support of the continent. Onshore, there are three main regions of volcanic activity–the Antarctic Peninsula, MBL, and the TAM. However, the presence of glacial cover in Antarctica hinders efforts to fully grasp its true extent. In an attempt to map subglacial volcanism, van Wyk de Vries et al. (2018) use a combination of bedrock elevation, aeromagnetic, aero-gravity, and satellite imagery data to identify conical edifices interpreted as volcanoes. The likelihood of a feature being a volcano is assessed based on the number of data sets–for the purpose of this study we filter the inventory to only include those which have a confidence factor >80% (Figure 13). Whilst

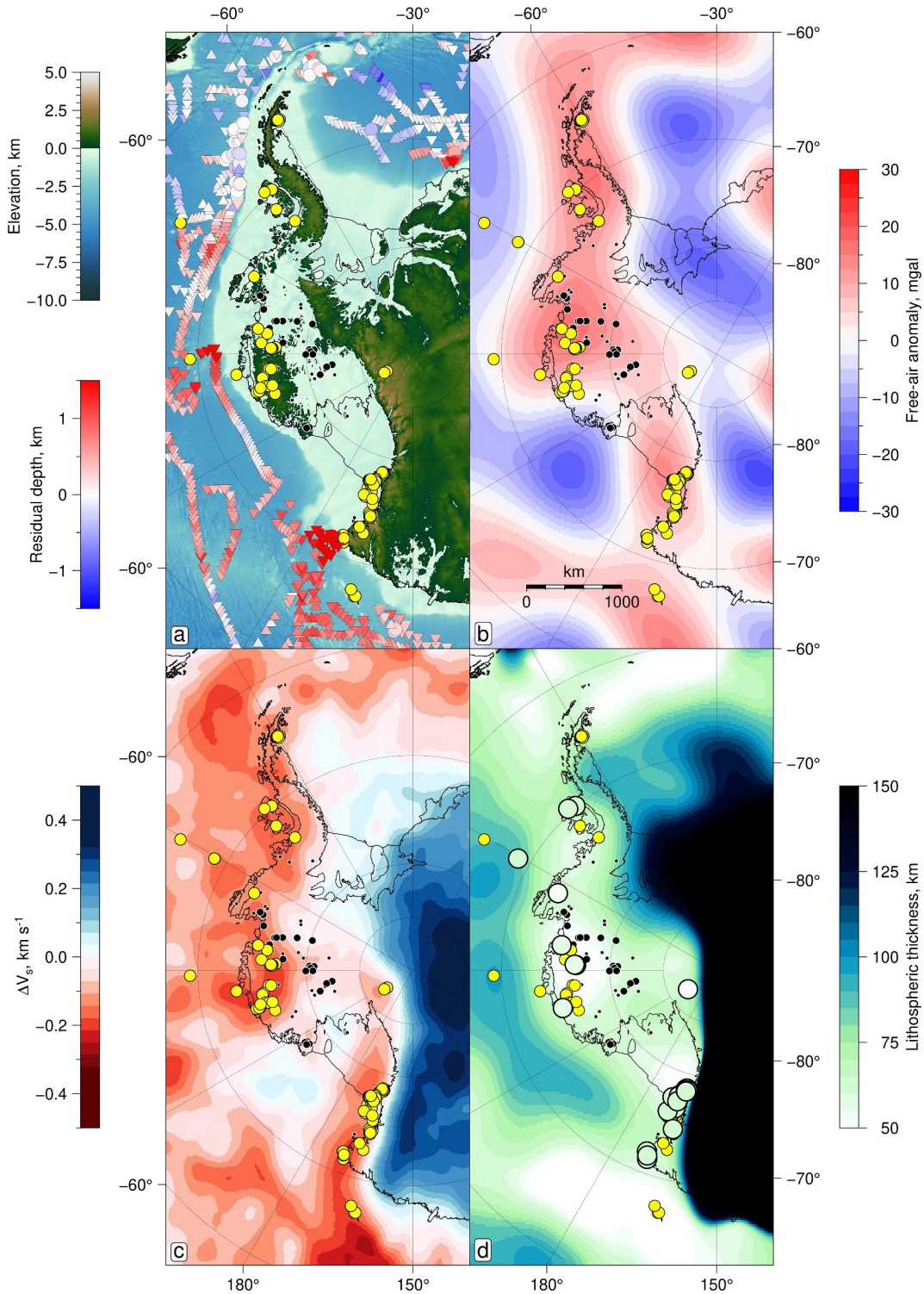

Figure 13. Dynamic support of West Antarctica. (a) Polar stereographic projection of West Antarctic topography. Colored circles/triangles = residual depth measurements as in Figure 8; yellow circles = location of known Neogene intraplate basaltic volcanism; black circles = subglacial edifices inferred as volcanoes with confidence factors exceeding 80% (small) and 90% (large) (van Wyk de Vries et al., 2018). (b) Free-air gravity anomaly bandpass filtered between l = 12–29 as per Figure 9. (c) ANT-20 relative shear-wave velocity anomaly averaged between 100–200 km (Lloyd et al., 2020). (d) Seismic lithospheric thickness derived from SL2013 (F. Richards, Hoggard, White, & Ghelichkhan, 2020). Colored circles = lithospheric thickness derived from REE modeling.

there is no way to guarantee that these represent Neogene volcanism, their proximity to known Cenozoic volcanic fields in West Antarctica implies they are likely co-genetic.

The distribution of known and inferred subglacial volcanism closely aligns with slow shear-wave velocity anomalies and positive free-air gravity anomalies, extending out southwards of MBL into the WARS (Figure 13). More specifically, by filtering out the long wavelength ($l < 12$) component of the free-air gravity anomaly, there is much greater correlation between volcanism in the WARS compared to just the non-hydrostatic free-air gravity anomaly (see Figure 1 for comparison).

Volcanic provinces in MBL and Victoria Land are adjacent to offshore oceanic residual depths of 1 km, supporting continuity of these observed dynamic swells onto the continent. In contrast, west of the Antarctica Peninsula, onshore volcanism is juxtaposed against negative residual depth measurements up to −500 m. Subduction of the Phoenix Plate eastward beneath the Antarctic Peninsula would typically be expected to result in draw down of the peninsula due to coupling between the subducting and overriding plates, exerting a downward buoyancy force on the overriding plate (Burgess & Moresi, 1999). However, there is considerable evidence for a slab window opening beneath the Peninsula, allowing warm mantle upwellings to provide dynamic support and a source for volcanism across the peninsula itself (Breitsprecher & Thorkelson, 2009; Eagles & Scott, 2014; Thorkelson, 1996).

Geochemically derived lithospheric thicknesses are within error of seismic estimates of lithospheric thickness, defined as the 1200°C isotherm (F. Richards, Hoggard, White, & Ghelichkhan, 2020) (Figure 13). Thinning of the lithosphere to this degree will have a notable impact on the topography above, which can be quantified using a simple isostatic balance such that uplift, U, is given by

$$U = \frac{(D_o - D_t)\rho_l - (D_o - D_t)\rho_a}{\rho_a}, \tag{6}$$

where lithoshperic and asthenospheric mantle densities are $\rho_l = 3.32$ Mg m^{-3} and $\rho_a = 3.25$ Mg m^{-3} respectively, and D_o and D_t are the original and thinned lithospheric thicknesses, respectively. Assuming that the ∼60 km thin lithosphere evident in both geochemical and geophysical data in MBL and the TAM was originally around ∼100 km thick as seen in the non-volcanic regions of West Antarctica, this would result in 1.125 km of dynamic topography, which could be further amplified by convective upwelling and temperature driven buoyancy in the asthenosphere.

4. Conclusions

We present a comprehensive suite of residual depth spot measurements ($n = 2105$) south of −50° determined from MCS and wide-angle refraction data. These observations build on global studies of dynamic topography and more precisely constrain the locations of dynamic swells and draw downs. Results contribute toward debates regarding the age of the east-central SS, with implausible residual depths ruling out origins predating Miocene times, unless the oceanic crust in the region is anomalously thick. The power spectrum associated with the spherical harmonic representation of residual depth remains robust, with maximum amplitude at spherical harmonic degree $l = 2$ and power out to and including $l = 40$.

By combining these residual depth observations with other geophysical and geochemical data we identify regions, both in the oceanic and continental realms, of dynamic support. Filtering of free-air gravity anomalies and calculation of residual shear-wave tomographic anomalies allows for correlations between mantle processes and residual depth anomalies. Such correlations are strongest when compared to data sampling the upper mantle, shallower than ∼500 km. The distribution of Neogene volcanism is coincident with mantle upwellings as imaged by tomographic models, and REE modeling of intraplate basalts provides an independent measure of lithospheric thickness, corroborating the association of mantle upwellings with thinned lithosphere and dynamic support. Robust constraints in the oceanic realm have provided a data set against which onshore Antarctic interpretations of dynamic support can be benchmarked, along with mantle convection and heat flux models.

Conflict of Interest

The authors declare no conflicts of interest relevant to this study.

Data Availability Statement

All seismic reflection data used in this study was obtained from the Seismic Data Library Service, an open Antarctic archive hosted by the Scientific Committee on Antarctic Research (http://SDLS.ogs.trieste.it). Specific lines used, as well as the resulting spot measurements of residual depth are provided as Supplementary Material both here and at Dunn et al. (2025). The database of basaltic samples was augmented from that provided in Ball et al. (2021).

The software used to perform isostatic corrections and calculate residual depth was obtained from Holdt et al. (2022) and is not currently publicly archived. Interested researchers should contact the authors directly for access.

Acknowledgments
ACAD is supported by the NERC C-CLEAR Doctoral Training Programme (NE/S007164/1) and St. John's College, Cambridge. We thank T. Jordan and D. Al-Attar for valued discussions and support. We also thank Matthew Fox, Lindsay Worthington, and one anonymous reviewer for their thoughtful and constructive feedback, which improved the clarity and quality of this work.

References

Allen, A. (1966). Seismic refraction investigations in the Scotia Sea.
Austermann, J., Pollard, D., Mitrovica, J. X., Moucha, R., Forte, A. M., DeConto, R. M., et al. (2015). The impact of dynamic topography change on Antarctic ice sheet stability during the mid-Pliocene warm period. *Geology*, *43*(10), 927–930. https://doi.org/10.1130/g36988.1
Ball, P., White, N., Maclennan, J., & Stephenson, S. (2021). Global influence of mantle temperature and plate thickness on intraplate volcanism. *Nature Communications*, *12*(1), 2045. https://doi.org/10.1038/s41467-021-22323-9
Bowin, C., Scheer, E., & Smith, W. (1986). Depth estimates from ratios of gravity, geoid, and gravity gradient anomalies. *Geophysics*, *51*(1), 123–136. https://doi.org/10.1190/1.1442025
Braun, J. (2010). The many surface expressions of mantle dynamics. *Nature Geoscience*, *3*(12), 825–833. https://doi.org/10.1038/ngeo1020
Breitsprecher, K., & Thorkelson, D. J. (2009). Neogene kinematic history of nazca–antarctic–phoenix slab windows beneath Patagonia and the antarctic peninsula. *Tectonophysics*, *464*(1–4), 10–20. https://doi.org/10.1016/j.tecto.2008.02.013
Brown, H., Colli, L., & Bunge, H.-P. (2022). Asthenospheric flow through the izanagi-pacific slab window and its influence on dynamic topography and intraplate volcanism in east Asia. *Frontiers in Earth Science*, *10*, 889907. https://doi.org/10.3389/feart.2022.889907
Burgess, & Moresi (1999). Modelling rates and distribution of subsidence due to dynamic topography over subducting slabs: Is it possible to identify dynamic topography from ancient strata? *Basin Research*, *11*(4), 305–314. https://doi.org/10.1046/j.1365-2117.1999.00102.x
Cao, W., Flament, N., Zahirovic, S., Williams, S., & Müller, R. D. (2019). The interplay of dynamic topography and eustasy on continental flooding in the late Paleozoic. *Tectonophysics*, *761*, 108–121. https://doi.org/10.1016/j.tecto.2019.04.018
Carlson, R., & Herrick, C. (1990). Densities and porosities in the oceanic crust and their variations with depth and age. *Journal of Geophysical Research*, *95*(B6), 9153–9170. https://doi.org/10.1029/jb095ib06p09153
Colli, L., Ghelichkhan, S., & Bunge, H.-P. (2016). On the ratio of dynamic topography and gravity anomalies in a dynamic Earth. *Geophysical Research Letters*, *43*(6), 2510–2516. https://doi.org/10.1002/2016gl067929
Conrad, C. P., & Husson, L. (2009). Influence of dynamic topography on sea level and its rate of change. *Lithosphere*, *1*(2), 110–120. https://doi.org/10.1130/l32.1
Conway-Jones, B. W., & White, N. (2022). Paleogene buried landscapes and climatic aberrations triggered by mantle plume activity. *Earth and Planetary Science Letters*, *593*, 117644. https://doi.org/10.1016/j.epsl.2022.117644
Croon, M. B., Cande, S. C., & Stock, J. M. (2008). Revised Pacific-Antarctic plate motions and geophysics of the Menard Fracture Zone. *Geochemistry, Geophysics, Geosystems*, *9*(7), Q07001. https://doi.org/10.1029/2008gc002019
Crosby, A., McKenzie, D., & Sclater, J. (2006). The relationship between depth, age and gravity in the oceans. *Geophysical Journal International*, *166*(2), 553–573. https://doi.org/10.1111/j.1365-246x.2006.03015.x
Czarnota, K., Hoggard, M., White, N., & Winterbourne, J. (2013). Spatial and temporal patterns of cenozoic dynamic topography around Australia. *Geochemistry, Geophysics, Geosystems*, *14*(3), 634–658. https://doi.org/10.1029/2012gc004392
DeMets, C., Gordon, R. G., & Argus, D. F. (2010). Geologically current plate motions. *Geophysical Journal International*, *181*(1), 1–80. https://doi.org/10.1111/j.1365-246x.2009.04491.x
Dunn, A., White, N., Larter, R., Slay, P., & Holdt, M. (2025). Supplementary material for "mantle dynamic topography of the ocean basins fringing antarctica". [Dataset]. *Zenodo*. https://doi.org/10.5281/zenodo.17234276
Eagles, G. (2010). The age and origin of the central Scotia Sea. *Geophysical Journal International*, *183*(2), 587–600. https://doi.org/10.1111/j.1365-246x.2010.04781.x
Eagles, G., Gohl, K., & Larter, R. D. (2004). High-resolution animated tectonic reconstruction of the South Pacific and West Antarctic Margin. *Geochemistry, Geophysics, Geosystems*, *5*(7), Q07002. https://doi.org/10.1029/2003gc000657
Eagles, G., Gohl, K., & Larter, R. D. (2009). Animated tectonic reconstruction of the Southern Pacific and alkaline volcanism at its convergent margins since Eocene times. *Tectonophysics*, *464*(1–4), 21–29. https://doi.org/10.1016/j.tecto.2007.10.005
Eagles, G., & Scott, B. G. (2014). Plate convergence west of Patagonia and the Antarctic Peninsula since 61 Ma. *Global and Planetary Change*, *123*, 189–198. https://doi.org/10.1016/j.gloplacha.2014.08.002
Ewing, J., Ludwig, W., Ewing, M., & Eittreim, S. (1971). Structure of the Scotia sea and Falkland plateau. *Journal of Geophysical Research*, *76*(29), 7118–7137. https://doi.org/10.1029/jb076i029p07118
Forte, A. M., & Mitrovica, J. X. (2001). Deep-mantle high-viscosity flow and thermochemical structure inferred from seismic and geodynamic data. *Nature*, *410*(6832), 1049–1056. https://doi.org/10.1038/35074000
Forte, Peltier, W., Dziewonski, A., & Woodward, R. (1993). Dynamic surface topography: A new interpretation based upon mantle flow models derived from seismic tomography. *Geophysical Research Letters*, *20*(3), 225–228. https://doi.org/10.1029/93gl00249
Forte, & Rowley, D. (2022). Earth's isostatic and dynamic topography—A critical perspective. *Geochemistry, Geophysics, Geosystems*, *23*(9), e2021GC009740. https://doi.org/10.1029/2021gc009740
Fox, M., Clinger, A., Smith, A. G., Cuffey, K., Shuster, D., & Herman, F. (2024). Antarctic peninsula glaciation patterns set by landscape evolution and dynamic topography. *Nature Geoscience*, *17*(1), 73–78. https://doi.org/10.1038/s41561-023-01336-7
Frey, F. A., Coffin, M., Wallace, P., Weis, D., Zhao, X., Wise Jr., S., et al. (2000). Origin and evolution of a submarine large igneous province: The Kerguelen Plateau and Broken Ridge, southern Indian Ocean. *Earth and Planetary Science Letters*, *176*(1), 73–89. https://doi.org/10.1016/s0012-821x(99)00315-5

Gille, S. T. (1994). Mean sea surface height of the Antarctic Circumpolar Current from Geosat data: Method and application. *Journal of Geophysical Research. Oceans*, *99*(C9), 18255–18273. https://doi.org/10.1029/94jc01172

Gille, S. T., McKee, D. C., & Martinson, D. G. (2016). Temporal changes in the Antarctic circumpolar current: Implications for the Antarctic continental shelves. *Oceanography*, *29*(4), 96–105. https://doi.org/10.5670/oceanog.2016.102

Golledge, N. R., Kowalewski, D. E., Naish, T. R., Levy, R. H., Fogwill, C. J., & Gasson, E. G. (2015). The multi-millennial Antarctic commitment to future sea-level rise. *Nature*, *526*(7573), 421–425. https://doi.org/10.1038/nature15706

Gurnis, M., & Muller, R. (2003). *Origin of the australian-Antarctic Discordance from an ancient slab and mantle wedge* (pp. 417–430). SPECIAL PAPERS-GEOLOGICAL SOCIETY OF AMERICA.

Hagedorn, B., Gersonde, R., Gohl, K., & Hubberten, H.-W. (2007). Petrology, geochemistry and K/Ar age constraints of the eastern De Gerlache Seamount alkaline basalts (ellingshausen Sea, southeast Pacific). *Polarforschung*, *76*(3), 87–94.

Hager, B., Clayton, R., Richards, M., Comer, R., & Dziewonski, A. (1985). Lower mantle heterogeneity, dynamic topography and the geoid. *Nature*, *313*(6003), 541–545. https://doi.org/10.1038/313541a0

Hager, B., & Richards, M. (1989). Long-wavelength variations in Earth's geoid: Physical models and dynamical implications. *Philosophical Transactions of the Royal Society of London. Series A, Mathematical and Physical Sciences*, *328*(1599), 309–327. https://doi.org/10.1098/rsta.1989.0038

Hart, S. R., Blijsztajn, J., & Craddock, C. (1995). Cenozoic volcanism in Antarctica: Jones mountains and Peter I Island. *Geochimica et Cosmochimica Acta*, *59*(16), 3379–3388. https://doi.org/10.1016/0016-7037(95)00212-i

Hasterok, D. P. (2010). *Thermal state of continental and oceanic lithosphere*. The University of Utah.

Hill, I. A., & Barker, P. F. (1980). Evidence for Miocene back-arc spreading in the central Scotia Sea. *Geophysical Journal International*, *63*(2), 427–440. https://doi.org/10.1111/j.1365-246x.1980.tb02630.x

Ho, T., Priestley, K., & Debayle, E. (2016). A global horizontal shear velocity model of the upper mantle from multimode Love wave measurements. *Geophysical Journal International*, *207*(1), 542–561. https://doi.org/10.1093/gji/ggw292

Hoggard, M., White, N., & Al-Attar, D. (2016). Global dynamic topography observations reveal limited influence of large-scale mantle flow. *Nature Geoscience*, *9*(6), 456–463. https://doi.org/10.1038/ngeo2709

Hoggard, M., Winterbourne, J., Czarnota, K., & White, N. (2017). Oceanic residual depth measurements, the plate cooling model, and global dynamic topography. *Journal of Geophysical Research: Solid Earth*, *122*(3), 2328–2372. https://doi.org/10.1002/2016jb013457

Holdt, M., White, N., & Richards, F. (2025). Revised oceanic plate cooling models. *Journal of Geophysical Research: Solid Earth*, *130*(7), e2024JB029890. https://doi.org/10.1029/2024jb029890

Holdt, M., White, N., Stephenson, S., & Conway-Jones, B. (2022). Densely sampled global dynamic topographic observations and their significance. *Journal of Geophysical Research: Solid Earth*, *127*, e2022JB024391. https://doi.org/10.1029/2022JB024391

Hole, M. (1988). Post-subduction alkaline volcanism along the Antarctic Peninsula. *Journal of the Geological Society*, *145*(6), 985–998. https://doi.org/10.1144/gsjgs.145.6.0985

Hole, M. (1990). Geochemical evolution of Pliocene-Recent post-subduction alkalic basalts from Seal Nunataks, Antarctic Peninsula. *Journal of Volcanology and Geothermal Research*, *40*(2), 149–167. https://doi.org/10.1016/0377-0273(90)90118-y

Hole, M., & LeMasurier, W. (1994). Tectonic controls on the geochemical composition of Cenozoic, mafic alkaline volcanic rocks from West Antarctica. *Contributions to Mineralogy and Petrology*, *117*(2), 187–202. https://doi.org/10.1007/bf00286842

Hole, M. J., Gibson, S. A., & Morris, M. C. (2023). Slab window–related magmatism as a probe for pyroxenite heterogeneities in the upper mantle. *Geology*, *51*(3), 268–272. https://doi.org/10.1130/g50687.1

Jennings, E. S., & Holland, T. J. (2015). A simple thermodynamic model for melting of peridotite in the system ncfmasocr. *Journal of Petrology*, *56*(5), 869–892. https://doi.org/10.1093/petrology/egv020

Jokat, W., Ritzmann, O., Reichert, C., & Hinz, K. (2004). Deep crustal structure of the continental margin off the Explora Escarpment and in the Lazarev Sea, East Antarctica. *Marine Geophysical Researches*, *25*(3–4), 283–304. https://doi.org/10.1007/s11001-005-1337-9

Jordan, T. H. (1975). The continental tectosphere. *Reviews of Geophysics*, *13*(3), 1–12. https://doi.org/10.1029/rg013i003p00001

Jordan, T. H. (1978). Composition and development of the continental tectosphere. *Nature*, *274*(5671), 544–548. https://doi.org/10.1038/274544a0

Katz, R. F., Spiegelman, M., & Langmuir, C. H. (2003). A new parameterization of hydrous mantle melting. *Geochemistry, Geophysics, Geosystems*, *4*(9). https://doi.org/10.1029/2002gc000433

Kennett, J. P. (1977). Cenozoic evolution of Antarctic glaciation, the circum-Antarctic Ocean, and their impact on global paleoceanography. *Journal of Geophysical Research*, *82*(27), 3843–3860. https://doi.org/10.1029/jc082i027p03843

Kipf, A., Hauff, F., Werner, R., Gohl, K., van den Bogaard, P., Hoernle, K., et al. (2014). Seamounts off the West Antarctic margin: A case for non-hotspot driven intraplate volcanism. *Gondwana Research*, *25*(4), 1660–1679. https://doi.org/10.1016/j.gr.2013.06.013

Kvas, A., Brockmann, J. M., Krauss, S., Schubert, T., Gruber, T., Meyer, U., et al. (2020). GOCO06s–a satellite-only global gravity field model. *Earth System Science Data Discussions*, 1–31.

Lindeque, A., Gohl, K., Henrys, S., Wobbe, F., & Davy, B. (2016). Seismic stratigraphy along the Amundsen Sea to Ross Sea continental rise: A cross-regional record of pre-glacial to glacial processes of the West Antarctic margin. *Palaeogeography, Palaeoclimatology, Palaeoecology*, *443*, 183–202. https://doi.org/10.1016/j.palaeo.2015.11.017

Livermore, R., McAdoo, D., & Marks, K. (1994). Scotia Sea tectonics from high-resolution satellite gravity. *Earth and Planetary Science Letters*, *123*(1–3), 255–268. https://doi.org/10.1016/0012-821x(94)90272-0

Lloyd, A. J., Wiens, D. A., Zhu, H., Tromp, J., Nyblade, A. A., Aster, R. C., et al. (2020). Seismic structure of the Antarctic upper mantle imaged with adjoint tomography. *Journal of Geophysical Research: Solid Earth*, *125*(3). https://doi.org/10.1029/2019jb017823

Lowe, M., Jordan, T., Ebbing, J., Koglin, N., Ruppel, A., Moorkamp, M., et al. (2024). Comparing geophysical inversion and petrophysical measurements for northern Victoria Land, Antarctica. *Geophysical Journal International*, *239*(1), 276–291. https://doi.org/10.1093/gji/ggae272

Martin, A. P., Price, R. C., Cooper, A. F., & McCammon, C. A. (2015). Petrogenesis of the rifted southern Victoria Land lithospheric mantle, Antarctica, inferred from petrography, geochemistry, thermobarometry and oxybarometry of peridotite and pyroxenite xenoliths from the Mount Morning eruptive centre. *Journal of Petrology*, *56*(1), 193–226. https://doi.org/10.1093/petrology/egu075

Martinson, D. G. (2012). Antarctic circumpolar current's role in the Antarctic ice system: An overview. *Palaeogeography, Palaeoclimatology, Palaeoecology*, *335*, 71–74. https://doi.org/10.1016/j.palaeo.2011.04.007

Matthews, S., Wong, K., Shorttle, O., Edmonds, M., & Maclennan, J. (2021). Do olivine crystallization temperatures faithfully record mantle temperature variability? *Geochemistry, Geophysics, Geosystems*, *22*(4), e2020GC009157. https://doi.org/10.1029/2020gc009157

Maus, S., Barckhausen, U., Berkenbosch, H., Bournas, N., Brozena, J., Childers, V., et al. (2009). EMAG2: A 2–arc min resolution Earth Magnetic Anomaly Grid compiled from satellite, airborne, and marine magnetic measurements. *Geochemistry, Geophysics, Geosystems*, *10*(8), Q08005. https://doi.org/10.1029/2009gc002471

McKenzie, D., & O'Nions, R. (1991). Partial melt distributions from inversion of rare earth element concentrations. *Journal of Petrology*, *32*(5), 1021–1091. https://doi.org/10.1093/petrology/32.5.1021

Menard, H. (1973). Depth anomalies and the bobbing motion of drifting islands. *Journal of Geophysical Research*, *78*(23), 5128–5137. https://doi.org/10.1029/jb078i023p05128

Morlighem, M., Rignot, E., Binder, T., Blankenship, D., Drews, R., Eagles, G., et al. (2020). Deep glacial troughs and stabilizing ridges unveiled beneath the margins of the Antarctic ice sheet. *Nature Geoscience*, *13*(2), 132–137. https://doi.org/10.1038/s41561-019-0510-8

Moucha, R., Forte, A. M., Mitrovica, J. X., Rowley, D. B., Quéré, S., Simmons, N. A., & Grand, S. P. (2008). Dynamic topography and long-term sea-level variations: There is no such thing as a stable continental platform. *Earth and Planetary Science Letters*, *271*(1–4), 101–108. https://doi.org/10.1016/j.epsl.2008.03.056

Moucha, R., Forte, A. M., Rowley, D. B., Mitrovica, J. X., Simmons, N. A., & Grand, S. P. (2009). Deep mantle forces and the uplift of the Colorado Plateau. *Geophysical Research Letters*, *36*(19). https://doi.org/10.1029/2009gl039778

Muller, R. D., Sdrolias, M., Gaina, C., Steinberger, B., & Heine, C. (2008). Long-term sea-level fluctuations driven by ocean basin dynamics. *Science*, *319*(5868), 1357–1362. https://doi.org/10.1126/science.1151540

Nowlin, W. D., Jr., & Klinck, J. M. (1986). The physics of the Antarctic circumpolar current. *Reviews of Geophysics*, *24*(3), 469–491. https://doi.org/10.1029/rg024i003p00469

Panasyuk, S. V., & Hager, B. H. (2000). Inversion for mantle viscosity profiles constrained by dynamic topography and the geoid, and their estimated errors. *Geophysical Journal International*, *143*(3), 821–836. https://doi.org/10.1046/j.0956-540x.2000.01286.x

Panter, K. S., Wilch, T., Smellie, J., Kyle, P., & McIntosh, W. (2021). Marie Byrd land and ellsworth land: Petrology.

Pappa, F., Ebbing, J., & Ferraccioli, F. (2019). Moho depths of Antarctica: Comparison of seismic, gravity, and isostatic results. *Geochemistry, Geophysics, Geosystems*, *20*(3), 1629–1645. https://doi.org/10.1029/2018gc008111

Parsons, B., & Daly, S. (1983). The relationship between surface topography, gravity anomalies, and temperature structure of convection. *Journal of Geophysical Research*, *88*(B2), 1129–1144. https://doi.org/10.1029/jb088ib02p01129

Parsons, B., & Sclater, J. G. (1977). An analysis of the variation of ocean floor bathymetry and heat flow with age. *Journal of Geophysical Research*, *82*(5), 803–827. https://doi.org/10.1029/jb082i005p00803

Paxman, G. J. G. (2023). Antarctic palaeotopography. In *The geochemistry and geophysics of the antarctic mantle*. Geological Society of London. https://doi.org/10.1144/M56-2020-7

Pekeris, C. L. (1935). Thermal convection in the interior of the Earth. *Geophysical Journal International*, *3*, 343–367. https://doi.org/10.1111/j.1365-246x.1935.tb01742.x

Prestvik, T., Barnes, C. G., Sundvoll, B., & Duncan, R. A. (1990). Petrology of Peter I øy (Peter I Island), West Antarctica. *Journal of Volcanology and Geothermal Research*, *44*(3–4), 315–338. https://doi.org/10.1016/0377-0273(90)90025-b

Richards, F., Hoggard, M., White, N., & Ghelichkhan, S. (2020). Quantifying the relationship between short-wavelength dynamic topography and thermomechanical structure of the upper mantle using calibrated parameterization of anelasticity. *Journal of Geophysical Research: Solid Earth*, *125*(9), e2019JB019062. https://doi.org/10.1029/2019jb019062

Richards, & Hager (1984). Geoid anomalies in a dynamic Earth. *Journal of Geophysical Research*, *89*(B7), 5987–6002. https://doi.org/10.1029/jb089ib07p05987

Richards, Hoggard, M., Cowton, L., & White, N. (2018). Reassessing the thermal structure of oceanic lithosphere with revised global inventories of basement depths and heat flow measurements. *Journal of Geophysical Research: Solid Earth*, *123*(10), 9136–9161. https://doi.org/10.1029/2018jb015998

Richards, Hoggard, M., Crosby, A., Ghelichkhan, S., & White, N. (2020). Structure and dynamics of the oceanic lithosphere-asthenosphere system. *Physics of the Earth and Planetary Interiors*, *309*, 106559. https://doi.org/10.1016/j.pepi.2020.106559

Rovere, A., Raymo, M. E., Mitrovica, J., Hearty, P. J., Oleary, M., & Inglis, J. (2014). The Mid-Pliocene sea-level conundrum: Glacial isostasy, eustasy and dynamic topography. *Earth and Planetary Science Letters*, *387*, 27–33. https://doi.org/10.1016/j.epsl.2013.10.030

Schaeffer, A., & Lebedev, S. (2013). Global shear speed structure of the upper mantle and transition zone. *Geophysical Journal International*, *194*(1), 417–449. https://doi.org/10.1093/gji/ggt095

Sempeéreé, J.-C., Palmer, J., Christie, D. M., Morgan, J. P., & Shor, A. N. (1991). Australian-Antarctic discordance. *Geology*, *19*(5), 429–432.

Seton, M., Müller, R. D., Zahirovic, S., Williams, S., Wright, N. M., Cannon, J., et al. (2020). A global data set of present-day oceanic crustal age and seafloor spreading parameters. *Geochemistry, Geophysics, Geosystems*, *21*(10), e2020GC009214. https://doi.org/10.1029/2020gc009214

Siddiquie, H., Gopala Rao, D., & Ramana, M. (2006). A geomorphologic, seismic and magnetic study of the astrid ridge, dronning maud land, Antarctica.

Siddiquie, H., Rao, D. G., & Ramana, M. (1988). Geology and structure of the Astrid Ridge, dronning maud land, Antarctica. *Paleoceanography*, *3*(5), 583–599. https://doi.org/10.1029/pa003i005p00583

Sokolov, S., & Rintoul, S. R. (2009). Circumpolar structure and distribution of the Antarctic circumpolar Current fronts: 1. Mean circumpolar paths. *Journal of Geophysical Research. Oceans*, *114*(C11), C11019. https://doi.org/10.1029/2008jc005108

Stein, C. A., & Stein, S. (1992). A model for the global variation in oceanic depth and heat flow with lithospheric age. *Nature*, *359*(6391), 123–129. https://doi.org/10.1038/359123a0

Steinberger, B. (2007). Effects of latent heat release at phase boundaries on flow in the Earth's mantle, phase boundary topography and dynamic topography at the Earth's surface. *Physics of the Earth and Planetary Interiors*, *164*(1–2), 2–20. https://doi.org/10.1016/j.pepi.2007.04.021

Steinberger, B., Conrad, C. P., Tutu, A. O., & Hoggard, M. J. (2019). On the amplitude of dynamic topography at spherical harmonic degree two. *Tectonophysics*, *760*, 221–228. https://doi.org/10.1016/j.tecto.2017.11.032

Stephenson, S. N., Hoggard, M. J., Holdt, M. C., & White, N. (2024). Continental residual topography extracted from global analysis of crustal structure. *Journal of Geophysical Research: Solid Earth*, *129*(4), e2023JB026735. https://doi.org/10.1029/2023jb026735

Thorkelson, D. J. (1996). Subduction of diverging plates and the principles of slab window formation. *Tectonophysics*, *255*(1–2), 47–63. https://doi.org/10.1016/0040-1951(95)00106-9

Toggweiler, J., & Bjornsson, H. (2000). Drake Passage and palaeoclimate. *Journal of Quaternary Science: Published for the Quaternary Research Association*, *15*(4), 319–328. https://doi.org/10.1002/1099-1417(200005)15:4<319::aid-jqs545>3.0.co;2-c

Toggweiler, J., & Samuels, B. (1995). Effect of Drake Passage on the global thermohaline circulation. *Deep Sea Research Part I: Oceanographic Research Papers*, *42*(4), 477–500. https://doi.org/10.1016/0967-0637(95)00012-u

van Wyk de Vries, M., Bingham, R. G., & Hein, A. S. (2018). A new volcanic province: An inventory of subglacial volcanoes in West Antarctica. In *Exploration of subsurface Antarctica: Uncovering past changes and modern processes*. Geological Society of. https://doi.org/10.1144/SP461.7

Winterbourne, J., Crosby, A., & White, N. (2009). Depth, age and dynamic topography of oceanic lithosphere beneath heavily sedimented Atlantic margins. *Earth and Planetary Science Letters*, *287*(1–2), 137–151. https://doi.org/10.1016/j.epsl.2009.08.019

Winterbourne, J., White, N., & Crosby, A. (2014). Accurate measurements of residual topography from the oceanic realm. *Tectonics*, *33*(6), 982–1015. https://doi.org/10.1002/2013tc003372

Wobbe, F., Gohl, K., Chambord, A., & Sutherland, R. (2012). Structure and breakup history of the rifted margin of West Antarctica in relation to Cretaceous separation from Zealandia and Bellingshausen plate motion. *Geochemistry, Geophysics, Geosystems*, *13*(4), Q04W12. https://doi.org/10.1029/2011gc003742

Yang, T., & Gurnis, M. (2016). Dynamic topography, gravity and the role of lateral viscosity variations from inversion of global mantle flow. *Geophysical Supplements to the Monthly Notices of the Royal Astronomical Society*, *207*(2), 1186–1202. https://doi.org/10.1093/gji/ggw335